Mapping single-cell atlases throughout Metazoa unravels cell type evolution

Alexander J. Tarashansky[1], Jacob M. Musser[2,§], Margarita Khariton[1,§], Pengyang Li[1], Detlev Arendt[2,3], Stephen R. Quake[1,4,5], Bo Wang[1,6*]

[1]Department of Bioengineering, Stanford University, Stanford, CA, USA.

[2]European Molecular Biology Laboratory, Developmental Biology Unit, Heidelberg, Germany.

[3]Centre for Organismal Studies, University of Heidelberg, Heidelberg, Germany.

[4]Department of Applied Physics, Stanford University, Stanford, CA, USA.

[5]Chan Zuckerberg Biohub, San Francisco, CA, USA.

[6]Department of Developmental Biology, Stanford University School of Medicine, Stanford, CA, USA.

[§]These authors contributed equally to this work.

*Correspondence: wangbo@stanford.edu.

Abstract

Comparing single-cell transcriptomic atlases from diverse organisms can elucidate the origins of cellular diversity and assist the annotation of new cell atlases. Yet, comparison between distant relatives is hindered by complex gene histories and diversifications in expression programs. Previously, we introduced the self-assembling manifold (SAM) algorithm to robustly reconstruct manifolds from single-cell data (Tarashansky et al., 2019). Here, we build on SAM to map cell atlas manifolds across species. This new method, SAMap, identifies homologous cell types with shared expression programs across distant species within phyla, even in complex examples where homologous tissues emerge from distinct germ layers. SAMap also finds many genes with more similar expression to their paralogs than their orthologs, suggesting paralog substitution may be more common in evolution than previously appreciated. Lastly, comparing species across animal phyla, spanning mouse to sponge, reveals ancient contractile and stem cell families, which may have arisen early in animal evolution.

Introduction

There is much ongoing success in producing single-cell transcriptomic atlases to investigate the cell type diversity within individual organisms (Regev et al., 2017). With the growing diversity of cell atlases across the tree of life (Briggs et al., 2018; Cao et al., 2019; Fincher et al., 2018; Hu et al., 2020; Musser et al., 2019; Plass et al., 2018; Siebert et al., 2019; Wagner et al., 2018), a new frontier is emerging: the use of cross-species cell type comparisons to unravel the origins of cellular diversity and uncover species-specific cellular innovations (Arendt et al., 2019; Shafer, 2019). Further, these comparisons promise to accelerate cell type annotation and discovery by transferring knowledge from well-studied model organisms to under-characterized animals.

However, recent comparative single-cell analyses are mostly limited to species within the same phylum (Baron et al., 2016; Geirsdottir et al., 2019; Sebé-Pedrós et al., 2018; Tosches et al., 2018). Comparisons across longer evolutionary distances and across phyla are challenging for two major reasons. First, gene regulatory programs diversify during evolution, diminishing the similarities in cell type specific gene expression patterns. Second, complex gene evolutionary history causes distantly related organisms to share few one-to-one gene orthologs (Nehrt et al., 2011), which are often relied upon for comparative studies (Briggs et al., 2018; Shafer, 2019). This effect is compounded by the growing evidence suggesting that paralogs may be more functionally similar than orthologs across species, due to differential gain (neo-functionalization), loss (non-functionalization), or partitioning (sub-functionalization) events among paralogs (Nehrt et al., 2011; Prince & Pickett, 2002; Stamboulian et al., 2020; Studer & Robinson-Rechavi, 2009).

57

58 Here, we present the Self-Assembling Manifold mapping (SAMap) algorithm to enable
59 mapping single-cell transcriptomes between phylogenetically remote species. SAMap
60 relaxes the constraints imposed by sequence orthology, using expression similarity
61 between mapped cells to infer the relative contributions of homologous genes, which in
62 turn refines the cell type mapping. In addition, SAMap uses a graph-based data
63 integration technique to identify reciprocally connected cell types across species with
64 greater robustness than previous single-cell data integration methods (Haghverdi et al.,
65 2018; Hie et al., 2019; Polański et al., 2019; Stuart et al., 2019).

66

67 Using SAMap, we compared seven whole-body cell atlases from species spanning animal
68 phylogeny, which have divergent transcriptomes and complex molecular homologies
69 (**Figure 1A-B** and **Supplementary Table 1**). We began with well-characterized cell types
70 in developing frog and fish embryos. We found broad concordance between
71 transcriptomic signatures and ontogenetic relationships, which validated our mapping
72 results, yet also detected striking examples of homologous cell types emerging from
73 different germ layers. We next extended the comparison to animals from the same phylum
74 but with highly divergent body plans, using a planarian flatworm and a parasitic blood
75 fluke, and found one-to-one homologies even between cell subtypes. Comparing all
76 seven species from sponge to mouse, we identified densely interconnected cell type
77 families broadly shared across animals, including contractile and stem cells, along with
78 their respective gene expression programs. Lastly, we noticed that homologous cell types
79 often exhibit differential expression of orthologs and similar expression of paralogs,

80 suggesting that the substitution and swapping of paralogs in cell types may be more
81 common in evolution than previously appreciated. Overall, our study represents an
82 important step towards analyzing the evolutionary origins of specialized cell types and
83 their associated gene expression programs in animals.

Results

The SAMap algorithm

SAMap iterates between two modules. The first module constructs a gene-gene bipartite graph with cross-species edges connecting homologous gene pairs, initially weighted by protein sequence similarity (**Figure 1C**). In the second module, SAMap uses the gene-gene graph to project the two single-cell transcriptomic datasets into a joint, lower-dimensional manifold representation, from which each cell's mutual cross-species neighbors are linked to stitch the cell atlases together (**Figure 1D**). Then, using the joint manifold, the expression correlations between homologous genes are computed and used to reweight the edges in the gene-gene homology graph in order to relax SAMap's initial dependence on sequence similarity. The new homology graph is used as input to the subsequent iteration of SAMap, and the algorithm continues until convergence, defined as when the cross-species mapping does not significantly change between iterations (**Figure 1E**).

This algorithm overcomes several challenges inherent to mapping single-cell transcriptomes between distantly related species. First, complex gene evolutionary history often results in many-to-many homologies with convoluted functional relationships (Briggs et al., 2018; Nehrt et al., 2011). SAMap accounts for this by using the full homology graph to project each dataset into both its own and its partner's respective principal component (PC) spaces, constructed by the SAM algorithm, which we previously developed to robustly and sensitively identify cell types (Tarashansky et al., 2019). The resulting within- and cross-species projections are concatenated to form the joint space.

107 For the cross-species projections, we translate each species' features into those of its
108 partner, with the expression for individual genes imputed as the weighted average of their
109 homologs specified in the gene-gene bipartite graph. Iteratively refining the homology
110 graph to only include positively correlated gene pairs prunes the many-to-many
111 homologies to only include genes that are expressed in the same mapped cell types.
112
113 Second, frequent gene losses and the acquisitions of new genes result in many cell type
114 gene expression signatures being species-specific, limiting the amount of information that
115 is comparable across species. Restricting the analysis of each dataset to only include
116 genes that are shared across species would result in a decreased ability to resolve cell
117 types and subtypes with many species-specific gene signatures. SAMap solves this
118 problem by constructing the joint space through the concatenation of within- and cross-
119 species projections, thus encoding all genes from both species.
120
121 Lastly, the evolution of expression programs gradually diminishes the similarity between
122 homologous cell types. To account for this effect, SAMap links cell types across species
123 while tolerating their differences. Cells are mapped by calculating each of their *k* mutual
124 nearest cross-species neighbors in the combined projection. To establish more robust
125 mutual connectivity, we integrate information from each cell's local, within-species
126 neighborhood (**Figure 1D**), overcoming the inherent stochasticity of cross-species
127 correlations. Two cells are thus defined as mutual nearest cross-species neighbors when
128 their respective neighborhoods have mutual connectivity. It is important to note that the
129 magnitude of connections is not directly calculated from their expression similarity,

130 allowing cell types with diverged expression profiles to be tightly linked if they are among
131 each other's closest cross-species neighbors.
132
133 ***Paralog substitutions are prevalent between homologous cell types in frog and fish***
134 We first applied SAMap to the *Xenopus* and zebrafish atlases, which both encompass
135 embryogenesis until early organogenesis (Briggs et al., 2018; Wagner et al., 2018).
136 Previous analysis had linked cell types between these two organisms by matching
137 ontogeny, thereby providing a reference for comparison. SAMap produced a combined
138 manifold with a high degree of cross-species alignment while maintaining high resolution
139 for distinguishing cell types in each species (**Figure 2A**). We measured the mapping
140 strength between cell types by calculating an alignment score (edge width in **Figure 2B**
141 and color map in **Figure 2C**), defined as the average number of mutual nearest cross-
142 species neighbors of each cell relative to the maximum possible number of neighbors.
143
144 SAMap revealed broad agreement between transcriptomic similarity and developmental
145 ontogeny, linking 26 out of 27 expected pairs based on previous annotations (**Figure 2B**
146 and **Supplementary Table 2**) (Briggs et al., 2018). The only exception is the embryonic
147 kidney (pronephric duct/mesenchyme), potentially indicating that their gene expression
148 programs have significantly diverged. In addition, SAMap succeeded in drawing parallels
149 between the development of homologous cell types and matched time points along
150 several cell lineages (**Figure 2C**). While the concordance was consistent across cell
151 types, we noticed that the exact progression of developmental timing can vary, suggesting
152 that SAMap can quantify heterochrony with cell type resolution.

153

154 SAMap also weakly linked several closely related cell types with different ontogeny. For
155 example, optic cells from both species are also connected to eye primordium, frog skeletal
156 muscles to fish presomitic mesoderm, and frog hindbrain to fish forebrain/midbrain.
157 Notable exceptions also included mapped secretory cell types that differ in their
158 developmental origin and even arise from different germ layers (black edges in **Figure**
159 **2B**). They are linked through a large set of genes including conserved transcription factors
160 (e.g., *foxa1* (Dubaissi et al., 2014), *grhl* (Miles et al., 2017)) and proteins involved in
161 vesicular protein trafficking (**Figure 2 – figure supplement 1**). This observation supports
162 the notion that cell types may be transcriptionally and evolutionarily related despite having
163 different developmental origins (Arendt et al., 2016).

164

165 To benchmark SAMap performance, we used Eggnog (Huerta-Cepas et al., 2019) to
166 define one-to-one vertebrate orthologs between fish and frog and fed these gene pairs
167 as input to several broadly used single-cell data integration methods, Seurat (Stuart et
168 al., 2019), Liger (Welch et al., 2019), Harmony (Korsunsky et al., 2019), Scanorama (Hie
169 et al., 2019), and BBKNN (Polański et al., 2019). We found that they failed to map the two
170 atlases, yielding minimal alignment between them (**Figure 2D** and **Figure 2 – figure**
171 **supplement 2**). We also compared the results when restricting SAMap to using the one-
172 to-one orthologs instead of the full homology graph. Even when removing the many-to-
173 many gene homologies and the iterative refinement of the homology graph, we identified
174 similar, albeit weaker, cell type mappings. This suggests that, at least for the frog and fish

175 comparison, SAMap's performance is owed in large part to its robust, atlas stitching
176 approach.
177
178 The key benefit of using the full homology graph is to enable the systematic identification
179 of gene paralogs that exhibit greater similarity in expression across species than their
180 corresponding orthologs. These events are expected to arise as the result of gene
181 duplications followed by diversification of the resulting in-paralogs (Studer & Robinson-
182 Rechavi, 2009). In addition, genetic compensation by transcriptional adaptation, where
183 loss-of-function mutations are balanced by upregulation of related genes with similar
184 sequences (El-Brolosy et al., 2019), could also result in this signature. In total, SAMap
185 selected 8,286 vertebrate orthologs and 7,093 eukaryotic paralogs, as enumerated by
186 Eggnog, for manifold alignment. Among these, 565 genes have markedly higher
187 expression correlations (correlation difference > 0.3) with their paralogs than their
188 orthologs (**Figure 2E** and **Figure 2 – figure supplement 3**), and 209 genes have
189 orthologs that are either completely absent or lowly-expressed with no cell-type specificity
190 (**Supplementary Table 3**), suggesting that they may have lost their functional roles at
191 some point and were compensated for by their paralogs. We term these events as
192 "paralog substitutions". SAMap linked an additional 297 homologous pairs not previously
193 annotated by orthology or paralogy, but which exhibited sequence similarity and high
194 expression correlations (>0.5 Pearson correlation). These likely represent unannotated
195 orthologs/paralogs or isofunctional, distantly related homologs (Gabaldón & Koonin,
196 2013). These results illustrate the potential of SAMap in leveraging single-cell gene
197 expression data for pruning the networks of homologous genes to identify evolutionary

198 substitution of paralogs and, more generally, identify non-orthologous gene pairs that may
199 perform similar functions in the cell types within which they are expressed.
200
201 ***Homologous cell types between two flatworm species with divergent body plans***
202 To test if we can identify homologous cell types in animals with radically different body
203 plans, we mapped the cell atlases of two flatworms, the planarian *Schmidtea*
204 *mediterranea* (Fincher et al., 2018), and the trematode *Schistosoma mansoni*, which we
205 collected recently (Li et al., 2020). They represent two distant lineages within the same
206 phylum but have remarkably distinct body plans and autecology (Laumer et al., 2015;
207 Littlewood & Waeschenbach, 2015). While planarians live in freshwater and are known
208 for their ability to regenerate (Reddien, 2018), schistosomes live as parasites in humans.
209 The degree to which cell types are conserved between them is unresolved, given the vast
210 phenotypic differences caused by the transition from free-living to parasitic habits
211 (Laumer et al., 2015).
212
213 SAMap revealed broad cell type homology between schistosomes and planarians. The
214 schistosome had cells mapped to the planarian stem cells, called neoblasts, as well as
215 most of the differentiated tissues: neural, muscle, intestine, epidermis, parenchymal,
216 protonephridia, and *cathepsin*$^{+}$ cells, the latter of which consists of cryptic cell types that,
217 until now, have only been found in planarians (Fincher et al., 2018) (**Figure 3A**). These
218 mappings are supported by both known cell type specific marker genes and numerous
219 homologous transcriptional regulators (**Figure 3B** and **Figure 3 – figure supplement 1**).
220

221 We next determined if cell type homologies exist at the subtype level. For this, we
222 compared the neoblasts, as planarian neoblasts are known to comprise populations of
223 pluripotent cells and tissue-specific progenitors (Fincher et al., 2018; Zeng et al., 2018).
224 By mapping the schistosome neoblasts to a planarian neoblast atlas (Zeng et al., 2018),
225 we found that the schistosome has a population of neoblasts (ε-cells (Wang et al., 2018))
226 that cluster with the planarian's pluripotent neoblasts, both expressing a common set of
227 TFs (e.g., *soxp2, unc4*, *pax6a*, *gcm1*) (**Figure 3C-D**). The ε-cells are closely associated
228 with juvenile development and lost in adult schistosomes (Wang et al., 2018), indicating
229 pluripotent stem cells may be a transient population restricted to their early developmental
230 stages. This is consistent with the fact that, whereas schistosomes can heal wounds, they
231 have limited regenerative ability (Wendt & Collins, 2016). SAMap also linked other
232 schistosome neoblast populations with planarian progenitors, including two populations
233 of schistosome neoblasts (denoted as μ (Tarashansky et al., 2019) and μ') to planarian
234 muscle progenitors, all of which express *myoD*, a canonical master regulator of
235 myogenesis (Scimone et al., 2017). These likely represent early and late muscle
236 progenitors, respectively, as μ-cells do not yet express differentiated muscle markers
237 such as *troponin*, whereas μ'-cells do (**Figure 3 – figure supplement 2).**
238

239 ***Cell type families spanning the animal tree of life***

240 To compare cell types across broader taxonomic scales, we extended our analysis to
241 include juvenile freshwater sponge (*Spongilla lacustris*) (Musser et al., 2019), adult *Hydra*
242 (*Hydra vulgaris*) (Siebert et al., 2019), and mouse (*Mus musculus*) embryogenesis
243 (Pijuan-Sala et al., 2019) atlases. In total, SAMap linked 1,051 cross-species pairs of cell

244 types, defined by the annotations used in each respective study. 95% of the cell type
245 pairs are supported by at least 40 enriched gene pairs, and 87% are supported by more
246 than 100 gene pairs, indicating that SAMap does not spuriously connect cell types with
247 limited overlap in expression profiles (**Figure 4A**).
248
249 We next extended the notion of cell type pairs to cell type trios, as mapped cell types gain
250 additional support if they share transitive relationships to other cell types through
251 independent mappings, forming cell type triangles among species. The transitivity of a
252 cell type pair (edge) or a cell type (node) can be quantified as the fraction of triads to
253 which they belong that form triangles (**Figure 4B**). The majority (81%) of cell type pairs
254 have non-zero transitivity independent of alignment score and the number of enriched
255 gene pairs (**Figure 4 – figure supplement 1-2**). Cell type pairs with fewer than 40
256 enriched gene pairs tend to have lower (<0.4) transitivity (**Figure 4 – figure supplement**
257 **2**). In addition, 16% of mapped cell type pairs have zero edge transitivity but non-zero
258 node transitivity, meaning that at least one of the cell types connects to only a single
259 member of an interconnected cell type group (**Figure 4C**). Such edges may be of lower
260 confidence as they should connect to other members of the same group and are thus
261 excluded from downstream analysis.
262
263 Among the interconnected groups of cell types, we identified families of contractile cells
264 and neural cells (**Figure 4D**). Both cell type families are highly transitive compared to the
265 overall graph transitivity (bootstrap p-value < $1x10^{-5}$), meaning that their constituent cell
266 types have more transitive edges within the group than outside the group (**Figure 4E**). In

267 addition, the dense, many-to-many connections within the contractile and neural families
268 are each supported by at least 40 enriched gene pairs (**Figure 4F**). Consistent with the
269 nerve net hypothesis suggesting a unified origin of neural cell types (Tosches & Arendt,
270 2013), the neural family includes vertebrate brain tissues, both bilaterian and cnidarian
271 neurons, cnidarian nematocytes that share the excitatory characteristics of neurons (Weir
272 et al., 2020), and *Spongilla* choanocytes and apopylar cells, both of which are not
273 considered as neurons but have been shown to express postsynaptic-like scaffolding
274 machinery (Musser et al., 2019; Wong et al., 2019). The contractile family includes
275 myocytes in bilaterian animals, *Hydra* myoepithelial cells that are known to have
276 contractile myofibrils (Buzgariu et al., 2015), and sponge pinacocytes and
277 myopeptidocytes, both of which have been implicated to play roles in contractility (Musser
278 et al., 2019; Sebé-Pedrós et al., 2018). In contrast to the families encompassing all seven
279 species, we also found a fully interconnected group that contains invertebrate pluripotent
280 stem cells, including planarian and schistosome neoblasts, *Hydra* interstitial cells, and
281 sponge archeocytes (Alié et al., 2015). The lack of one-to-one connections across phyla
282 is in keeping with recent hypotheses that ancestral cell types diversified into families of
283 cell types after speciation events (Arendt et al., 2016, 2019). Our findings thus suggest
284 that these cell type families diversified early in animal evolution.
285
286 ***Transcriptomic signatures of cell type families***
287 The high interconnectedness between cell types across broad taxonomic scales suggests
288 that they should share ancestral transcriptional programs (Arendt et al., 2016; Tosches
289 et al., 2018). SAMap identified broad transcriptomic similarity between bilaterian and non-

290 bilaterian contractile cells that extends beyond the core contractile apparatus. It links a
291 total of 23,601 gene pairs, connecting 5,471 unique genes, which are enriched in at least
292 one contractile cell type pair. Performing functional enrichment analysis on these genes,
293 we found cytoskeleton and signal transduction functions to be enriched (p-value < 10^{-3})
294 based on the KOG functional classifications (Tatusov et al., 2003) assigned by Eggnog
295 (**Figure 5A**). These genes include orthology groups spanning diverse functional roles in
296 contractile cells, including actin regulation, cell adhesion and stability, and signaling
297 (**Figure 5B** and **Supplementary Table 4**), indicating that contractile cells were likely
298 multifunctional near the beginning of animal evolution.
299
300 We also identified several transcriptional regulators shared among contractile cells
301 (**Figure 5B**). Previously known core regulators involved in myocyte specification (Brunet
302 et al., 2016) were enriched only in bilaterian (e.g., *myod*, and *tcf4/E12*) or vertebrate
303 contractile cells (e.g., *mef2*). In contrast, we found homologs of Muscle Lim Protein (*Csrp*)
304 and Forkhead Box Group 1 (Larroux et al., 2008) enriched in contractile cells from all
305 seven species. The Fox proteins included FoxC, which is known to regulate cardiac
306 muscle identity in vertebrates (Brunet et al., 2016) and is contractile-specific in all species
307 except schistosome and *Spongilla*. Notably, we also identified FoxG orthologs to be
308 enriched in three of the four invertebrates (**Figure 5 – figure supplement 1**), suggesting
309 that FoxG may play an underappreciated role in contractile cell specification outside
310 vertebrates.
311

312 For the family of invertebrate stem cells, we identified 3,343 genes that are enriched in at
313 least one cell type pair and observed significant enrichment (p-value < 10^{-3}) of genes
314 involved in translational regulation such as RNA processing, translation, and post-
315 translational modification (**Figure 5C**). These genes form 979 orthology groups, 17% of
316 which are enriched in all cell types of this family (**Supplementary Table 4**). Importantly,
317 other stem cell populations in *Hydra* and planarian lineage-restricted neoblasts have
318 significantly reduced expression of these genes (**Figure 5D**). These results suggest that
319 SAMap identified a large, deeply conserved gene module specifically associated with
320 multipotency.
321

322 **Discussion**

323 Cell types evolve as their gene expression programs change either as integrated units or
324 via evolutionary splitting that results in separate derived programs. While this notion of
325 coupled cellular and molecular evolution has gained significant traction in the past years,
326 systematically comparing cell type-specific gene expression programs across species
327 has remained a challenging problem. Here, we map single-cell atlases between
328 evolutionarily distant species in a manner that accounts for the complexity of gene
329 evolution. SAMap aligns cell atlases in two mutually reinforcing directions, mapping both
330 the genes and the cells, with each feeding back into the other. This method allows us to
331 identify one-to-one cell type concordance between animals in the same phylum, whereas
332 between phyla, we observe interconnected cell types forming distinct families. These
333 findings support the notion that cell types evolve via hierarchical diversification (Arendt et
334 al., 2019), resulting in cell type families composed of evolutionarily related cell types

335 sharing a regulatory gene expression program that originated in their common ancestor.
336 One-to-one cell type homologies should exist only if no further cell type diversification has
337 occurred since the speciation.
338
339 In parallel, SAMap systematically identifies instances where paralogs exhibit greater
340 expression similarity than orthologs across species. Paralog substitution likely occurs due
341 to differential loss or retention of cell type-specific expression patterns of genes that were
342 duplicated in the common ancestor (Studer & Robinson-Rechavi, 2009). Alternatively,
343 paralog substitutions could arise due to compensating upregulation of paralogs following
344 a loss-of-function mutation acquired by an ortholog (El-Brolosy et al., 2019). While the
345 analysis presented here focuses on comparisons between two species, incorporating
346 multiple species into a single analysis that also accounts for their phylogenetic
347 relatedness could enable determining the specific order of paralog substitutions,
348 associated cell type diversification events, and the mechanism by which they arose.
349 However, this would require cell atlases that consistently sample key branching points
350 along the tree of life. Nevertheless, identifying lineage-specific paralog substitution
351 signatures should be accessible in extensively studied vertebrate single-cell atlases, as
352 the vertebrate clade is where existing data and knowledge are most concentrated.
353
354 Besides applications in evolutionary biology, we anticipate SAMap can catalyze the
355 annotation of new cell atlases from non-model organisms, which often represents a
356 substantial bottleneck requiring extensive manual curation and prior knowledge. Its ability
357 to use the existing atlases to inform the annotation of cell types in related species will

358 keep improving as more datasets become available to better sample the diversity of cell
359 types. Moreover, our approach allows leveraging existing and forthcoming single-cell
360 gene expression data to predict functionally similar gene homologs, which can serve as
361 guideposts for mechanistic molecular studies.
362

Materials and Methods

Data and Code Availability

- The source code for SAMap is publicly available at Github (https://github.com/atarashansky/SAMap), along with the code to perform the analysis and generate the figures.
- The datasets analyzed in this study are detailed in **Supplementary Table 1** with their accessions, and annotations provided.

The SAMap Algorithm

The SAMap algorithm contains three major steps: preprocessing, mutual nearest neighborhood alignment, and gene-gene correlation initialization. The latter two are repeated for three iterations, by default, to balance alignment performance and computational runtime. SAMap runs up to one hour on an average desktop computer for 200,000 total cells.

1. Preprocessing.

1.1. Generate gene homology graph via reciprocal BLAST.

We first construct a gene-gene bipartite graph between two species by performing reciprocal BLAST of their respective transcriptomes using *tblastx*, or proteomes using *blastp*. *tblastn* and *blastx* are used for BLAST between proteome and transcriptome. When a pair of genes share multiple High Scoring Pairs (HSPs), which are local regions

385 of matching sequences, we use the HSP with the highest bit score to measure homology.
386 Only pairs with E-value < 10^{-6} are included in the graph.
387
388 Here we define similarity using BLAST, though SAMap is compatible with other protein
389 homology detection methods (e.g. HMMER (Eddy, 2008)) or orthology inference tools
390 (e.g. OrthoClust (Yan et al., 2014) and Eggnog (Huerta-Cepas et al., 2019)). While each
391 of these methods has known strengths and limitations, BLAST is chosen for its broad
392 usage, technical convenience, and compatibility with low-quality transcriptomes.
393
394 We encode the BLAST results into two triangular adjacency matrices, A and B, each
395 containing bit scores in one BLAST direction. We combine A and B to form a gene-gene
396 adjacency matrix G. After symmetrizing G, we remove edges that only appear in one
397 direction: $G = Recip(\frac{1}{2}[(A+B)+(A+B)^T]) \in \Re^{m_1+m_2 \times m_1+m_2}$, where $Recip$ only keeps
398 reciprocal edges, and m_1 and m_2 are the number of genes of the two species,
399 respectively. To filter out relatively weak homologies, we also remove edges where $G_{ab} <$
400 $0.25 \max_b(G_{ab})$. Edge weights are then normalized by the maximum edge weight for each
401 gene and transformed by a hyperbolic tangent function to increase discriminatory power
402 between low and high edge weights, $\hat{G}_{ab} = 0.5 + 0.5\, tanh\, (10 G_{ab}/\max_b(G_{ab}) - 5)$.
403
404 *1.2. Construct manifolds for each cell atlas separately using the SAM algorithm.*
405 The scRNAseq datasets are normalized such that each cell has a total number of raw
406 counts equal to the median size of single-cell libraries. Gene expressions are then log-
407 normalized with the addition of a pseudocount of 1. Genes expressed (i.e.,$log_2(D+1) >$

408 1) in greater than 96% of cells are filtered out. SAM is run using the following parameters:
409 *preprocessing = 'StandardScaler'*, *weight_PCs = False*, *k = 20*, and *npcs = 150*. A detailed
410 description of parameters is provided previously (Tarashansky et al., 2019). SAM outputs
411 N_1 and N_2, which are directed adjacency matrices that encode *k*-nearest neighbor graphs
412 for the two datasets, respectively.
413
414 SAM only includes the top 3,000 genes ranked by SAM weights and the first 150 principal
415 components (PCs) in the default mode to reduce computational complexity. However,
416 downstream mapping requires PC loadings for all genes. Thus, in the final iteration of
417 SAM, we run PCA on all genes and take the top 300 PCs. This step generates a loading
418 matrix for each species i, $L_i \in \Re^{300 \times m_i}$.
419
420 *2. Mutual nearest neighborhood alignment.*
421 *2.1. Transform feature spaces between species.*
422 For the gene expression matrices $Z_i \in \Re^{n_i \times m_i}$, where n and m are the number of cells
423 and genes respectively, we first zero the expression of genes that do not have an edge
424 in $\hat{G}$ and standardize the expression matrices such that each gene has zero mean and
425 unit variance, yielding $\tilde{Z}_i$. $\hat{G}$ represents a bipartite graph in the form of $\hat{G} =$
426 $\begin{bmatrix} 0_{m_1,m_1} & H \in \Re^{m_1 \times m_2} \\ H^T \in \Re^{m_2 \times m_1} & 0_{m_2,m_2} \end{bmatrix}$, where $0_{m,m}$ is $m \times m$ zero matrix and H is the biadjacency
427 matrix. Letting $H_1 = H$ and $H_2 = H^T$ encoding directed edges from species 1 to 2 and 2
428 to 1, respectively, we normalize the biadjacency matrix H_i such that each row sums to 1:
429 $\widehat{H}_i = SumNorm(H_i) \in \Re^{m_i \times m_j}$, where the $SumNorm$ function normalizes the rows to sum

430 to 1. The feature spaces can be transformed between the two species via weighted
431 averaging of gene expression, $\tilde{Z}_{ij} = \tilde{Z}_i \hat{H}_i$.
432
433 *2.2. Project single-cell gene expressions into a joint PC space.*
434 We project the expression data from two species into a joint PC space (Barkas et al.,
435 2019), $P_i = \tilde{Z}_i {L_i}^T$ and $P_{ij} = \tilde{Z}_{ij} {L_j}^T$. We then horizontally concatenate the principal
436 components P_i and P_{ij} to form $\hat{P}_i \in \Re^{n_i \times 600}$.
437
438 *2.3. Calculate k-nearest cross-species neighbors for all cells.*
439 Using the joint PCs, $\hat{P}_i$, we identify for each cell the k-nearest neighbors in the other
440 dataset using cosine similarity ($k = 20$ by default). Neighbors are identified using the
441 *hnswlib* library, a fast approximate nearest-neighbor search algorithm (Malkov &
442 Yashunin, 2020). This outputs two directed biadjacency matrices $C_i \in \Re^{n_i \times n_j}$ for $(i, j) =$
443 $(1,2)\ or\ (2,1)$ with edge weights equal to the cosine similarity between the PCs.
444
445 *2.4. Apply the graph-coarsening mapping kernel to identify cross-species mutual nearest*
446 *neighborhoods.*
447 To increase the stringency and confidence of mapping, we only rely on cells that are
448 *mutual* nearest cross-species neighbors, which are typically defined as two cells
449 reciprocally connected to one another (Haghverdi et al., 2018). However, due to the noise
450 in cell-cell correlations and stochasticity in the kNN algorithms, cross-species neighbors
451 are often randomly assigned from a pool of cells that appear equally similar, decreasing
452 the likelihood of mutual connectivity between individual cells even if they have similar

453 expression profiles. To overcome this limitation, we integrate information from each cell's
454 local neighborhood to establish more robust mutual connectivity between cells across
455 species. Two cells are thus defined as mutual nearest cross-species neighbors when their
456 respective neighborhoods have mutual connectivity.
457
458 Specifically, the nearest neighbor graphs N_i calculated in step 1.2 are used to calculate
459 the neighbors of cells t_i hops away along outgoing edges: $\bar{N}_i = {N_i}^{t_i}$, where $\bar{N}_i$ are
460 adjacency matrices that contain the number of paths connecting two cells t_i hops away,
461 for $i = 1\ or\ 2$. t_i determines the length-scale over which we integrate incoming edges for
462 species i. Its default value is 2 if the dataset size is less than 20,000 cells and 3 otherwise.
463 However, cells within tight clusters may have spurious edges connecting to other parts of
464 the manifold only a few hops away. To avoid integrating neighborhood information outside
465 this local structure, we use the Leiden algorithm (Traag et al., 2019) to cluster the graph
466 and identify a local neighborhood size for each cell (the resolution parameter is set to 3
467 by default). If cell a belongs to cluster c_a, then its neighborhood size is $l_a = |c_a|$. For each
468 row a in $\bar{N}_i$ we only keep the l_a geodesically closest cells, letting the pruned graph be
469 denoted as $\widehat{N}_i$.
470
471 Edges outgoing from cell a_i in species i are encoded in the corresponding row in the
472 adjacency matrix: C_{i,a_i}. We compute the fraction of the outgoing edges from each cell that
473 target the local neighborhood of a cell in the other species: $\tilde{C}_{i,a_i b_j} = \sum_{c \in X_{j,b_j}} C_{i,a_i c}$, where
474 X_{j,b_j} is the set of cells in the neighborhood of cell b_j in species j and $\tilde{C}_{i,a_i b_j}$ is the fraction

of outgoing edges from cell a_i in species i targeting the neighborhood of cell b_j in species j.

To reduce the density of $\tilde{C}_i$ so as to satisfy computational memory constraints, we remove edges with weight less than 0.1. Finally, we apply the mutual nearest neighborhood criterion by taking the element-wise, geometric mean of the two directed bipartite graphs: $\tilde{C} = \sqrt{\tilde{C}_1 \circ \tilde{C}_2}$. This operation ensures that only bidirectional edges are preserved, as small edge weights in either direction results in small geometric means.

2.5. Assign the k-nearest cross-species neighborhoods for each cell and update edge weights in the gene homology graph.

Given the mutual nearest neighborhoods $\tilde{C} \in \Re^{n_1 \times n_2}$, we select the k nearest neighborhoods for each cell in both directions to update the directed biadjacency matrices C_1 and C_2: $C_1 = KNN(\tilde{C}, k)$ and $C_2 = KNN(\tilde{C}^T, k)$, with $k = 20$ by default.

2.6. Stitch the manifolds.

We use C_1 and C_2 to combine the manifolds N_1 and N_2 into a unified graph. We first weight the edges in N_1 and N_2 to account for the number of shared cross-species neighbors by computing the one-mode projections of C_1 and C_2. In addition, for cells with strong cross-species alignment, we attenuate the weight of their within-species edges. For cells with little to no cross-species alignment, their within-species are kept the same to ensure that the local topological information around cells with no alignment is preserved.

Specifically, we use N_1 and N_2 to mask the edges in the one-mode projections, $\widetilde{N}_1 = U(N_1) \circ (Norm(C_1)Norm(C_2))$ and $\widetilde{N}_2 = U(N_2) \circ (Norm(C_2)Norm(C_1))$, where $U(E)$ sets all edge weights in graph E to 1 and $Norm$ normalizes the outgoing edges from each cell to sum to 1. The minimum edge weight is set to be 0.3 to ensure that neighbors in the original manifolds with no shared cross-species neighbors still retain connectivity: $\widetilde{N}_{1,ij} = min(0.3, \widetilde{N}_{1,ij})$ and $\widetilde{N}_{2,ij} = min(0.3, \widetilde{N}_{2,ij})$ for all edges (i, j). We then scale the within-species edges from cell i by the total weight of its cross-species edges: $\widetilde{N}_{1,i} = (1 - \frac{1}{k}\sum_{j=1}^{n_2} C_{1,ij})\widetilde{N}_{1,i}$ and $\widetilde{N}_{2,i} = (1 - \frac{1}{k}\sum_{j=1}^{n_1} C_{2,ij})\widetilde{N}_{2,i}$. Finally, the within- and cross-species graphs are stitched together to form the combined nearest neighbor graph N: $N = [\widetilde{N}_1 \oplus C_1] \oplus [C_2 \oplus \widetilde{N}_2]$. The overall alignment score between species 1 and 2 is defined as $S = \frac{1}{n_1+n_2}(\sum_{i=1}^{n_1}\sum_{j=1}^{n_2} C_{1,ij} + \sum_{i=1}^{n_2}\sum_{j=1}^{n_1} C_{2,ij})$.

3. Gene-gene correlation initialization.

3.1. Update edge weights in the gene-gene bipartite graph with expression correlations.

To compute correlations between gene pairs, we first transfer expressions from one species to the other: $\bar{Z}_{i,n_i m_j} = C_{i,n_i} Z_{j,m_j}$, where $\bar{Z}_{i,n_i m_j}$ is the imputed expressions of gene m_j from species j for cell n_i in species i, and C_{i,n_i} is row n_i of the biadjacency matrix encoding the cross-species neighbors of cell n_i in species i, all for $(i, j) = (1,2)$ and $(2,1)$. We similarly use the manifolds constructed by SAM to smooth the within-species gene expressions using kNN averaging: $\bar{Z}_{j,m_j} = N_{j,m_j} Z_{j,m_j}$, where N_j is the nearest-neighbor graph for species j. We then concatenate the within- and cross-species gene expressions such that the expression of gene m_j from species j in both species is $\bar{Z}_{m_j} = \bar{Z}_{i,m_j} \oplus \bar{Z}_{j,m_j}$.

For all gene pairs in the unpruned homology graph generated in step 1.1., $\hat{G}$, we compute their correlations, $\hat{G}_{ab} := \theta(0) Corr(\bar{Z}_a, \bar{Z}_b)$, where $\theta(0)$ is a Heaviside step function centered at 0 to set negative correlations to zero. We then use the expression correlations to update the corresponding edge weights in $\hat{G}$, which are again normalized through $\hat{G}_{ab} = 0.5 + 0.5\, tanh\, (10\hat{G}_{ab}/\max_b(\hat{G}_{ab}) - 5)$.

Annotation of cell atlases

To annotate the primary zebrafish and *Xenopus* cell types, the cell subtype annotations provided by the original publications (Briggs et al., 2018; Wagner et al., 2018) are coarsened using a combination of the manual matching and developmental hierarchies. For example, as “heart - mature”, “heart - hoxd9a”, “heart”, and “heart field” in zebrafish are all manually matched to “cardiac mesoderm” in *Xenopus*, we label these cells as “heart”. In cases where the matching is insufficient to coarsen the annotations, we use the provided developmental trees to name a group of terminal cell subtypes by their common ontogenic ancestor. The annotations provided by their respective studies were used to label the cells in the *Spongilla*, *Hydra*, and mouse atlases. To annotate the schistosome cells, we used known marker genes to annotate the main schistosome tissue types (Li et al., 2020). Annotations for all single cells in all datasets are provided in **Supplementary Table 1**.

Visualization

The combined manifold N is embedded into 2D projections using UMAP implemented in

543 the scanpy package (Wolf et al., 2018) by *scanpy.tl.umap* with the parameter *min_dist* =
544 0.1. The sankeyD3 package (https://rdrr.io/github/fbreitwieser/sankeyD3/man/sankeyD3-
545 package.html) in R is used to generate the sankey plots. Edge thickness corresponds to
546 the alignment score between mapped cell types. The alignment score between cell types
547 a and b is defined as $s_{ab} = \frac{1}{|c_a|+|c_b|}(\sum_{i \in c_a}\sum_{j \in c_b} C_{1,ij} + \sum_{i \in c_b}\sum_{j \in c_a} C_{2,ij})$, where c_a and c_b
548 are the set of cells in cell types a and b, respectively. Cell type pairs with alignment score
549 less than z are filtered out. By default, z is set to be 0.1. Cell types that did not cluster
550 properly in their respective manifolds were omitted from the sankey plot. In the zebrafish-
551 *Xenopus* comparison, we excluded heart, germline, and olfactory placode cells from both
552 species because they did not cluster in the *Xenopus* atlas. Similarly, the iridoblast,
553 epiphysis, *nanog*+, apoptotic-like, and forerunner cells were excluded because they did
554 not cluster in the zebrafish atlas.
555
556 The network graphs in **Figure 4D** are generated using the *networkx* package
557 (https://networkx.github.io) in python. To focus on densely connected cell type groups,
558 we filter out cell type pairs with alignment score less than 0.05.
559
560 ***Identification of gene pairs that drive cell type mappings***
561 We define g_1 and g_2 to contain SAMap-linked genes from species 1 and 2, respectively.
562 Note that a gene may appear multiple times as SAMap allows for one-to-many homology.
563 Let $X_{a_1 b_2}$ denote the set of all cells with cross species edges between cell types a_1 and
564 b_2. We calculate the average standardized expression of all cells from species i that are
565 in $X_{a_1 b_2}$: $Y_{i,g_i} = \frac{1}{|\{x, x \in X_{a_1 b_2}\}|}\sum_{x \in X_{a_1 b_2}} \tilde{Z}_{i,x,g_i}$, where $\tilde{Z}_{i,x,g_i} \in \Re^{|g_i|}$ is the standardized

566 expression of genes g_i in cell x. The correlation between Y_{1,g_1} and Y_{2,g_2} can be written as
567 $Corr(Y_{1,g_1}, Y_{2,g_2}) = \sum_{j=1}^{|g_1|} S(Y_{1,g_1})_j \circ S(Y_{2,g_2})_j$, where $S(Z)$ standardizes vector Z to have
568 zero mean and unit variance. We use the summand to identify gene pairs that contribute
569 most positively to the correlation. We assign each gene pair a score: $h_g = T(S(Y_{1,g_1})) \circ$
570 $T(S(Y_{2,g_2}))$, where $T(Z)$ sets negative values in vector Z to zero in order to ignore lowly-
571 expressed genes. To be inclusive, we begin with the top 1,000 gene pairs according to
572 h_g and filter out gene pairs in which one or both of the genes are not differentially
573 expressed in their respective cell types (p-value > 10^{-2}), have less than 0.2 SAM weight,
574 or are expressed in fewer than 5% of the cells in the cluster. The differential expression
575 of each gene in each cell type is calculated using the Wilcoxon rank-sum test
576 implemented in the *scanpy* function *scanpy.tl.rank_genes_groups*.
577
578 ***Orthology group assignment***
579 We used the Eggnog mapper (v5.0) (Huerta-Cepas et al., 2019) to assign each gene to
580 an orthology group with default parameters. For the zebrafish-to-*Xenopus* mapping,
581 genes are considered paralogs if they map to the same eukaryotic orthology group and
582 orthologs if they map to the same vertebrate orthology group. For the pan-species
583 analysis, we group genes from all species with overlapping orthology assignments. In
584 **Figure 5B**, each column corresponds to one of these groups. As each group may contain
585 multiple genes from each species, we present the expression of the gene with the highest
586 enrichment score per species. All gene names and corresponding orthology groups are
587 reported in **Supplementary Table 4**.
588

589 ***Phylogenetic reconstruction of gene trees***

590 We generate gene trees to validate the identity of genes involved in putative examples of
591 paralog substitution and of *Fox* and *Csrp* transcriptional regulators that are identified as
592 enriched in contractile cells. For this, we first gather protein sequences from potential
593 homologs using the eggnog version 5.0 orthology database (Huerta-Cepas et al., 2019).
594 For the *Fox* and *Csrp* phylogenies, we include all Fox clade I (Larroux et al., 2008) and
595 Csrp/Crip homologs, respectively, from the seven species included in our study.

596

597 Alignment of protein sequences is performed with Clustal Omega version 1.2.4 using
598 default settings as implemented on the EMBL EBI web services platform (Madeira et al.,
599 2019). Maximum likelihood tree reconstruction is performed using IQ-TREE version
600 1.6.12 (Nguyen et al., 2015) with the ModelFinder Plus option (Kalyaanamoorthy et al.,
601 2017). For the *Csrp* tree, we perform 1,000 nonparametric bootstrap replicates to assess
602 node support. For *Fox*, we utilize the ultrafast bootstrap support option with 1,000
603 replicates. For each gene tree we choose the model that minimizes the Bayesian
604 Information Criterion (BIC) score in ModelFinder. This results in selection of the following
605 models: DCMut+R4 (*Csrp*) and VT+F+R5 (*Fox*). The final consensus trees are visualized
606 and rendered using the ete3 v3.1.1 python toolkit (Huerta-Cepas et al., 2016) and the
607 Interactive Tree of Life v4 (Letunic & Bork, 2019).

608

609 ***KOG functional annotation and enrichment analysis***

610 Using the eggnog mapper, KOG functional annotations are transferred to individual
611 transcripts from their assigned orthology group. For enrichment analysis, all genes

612 enriched in the set of cell type pairs of interest are lumped to form the target set for each
613 species. For example, the target set for *Spongilla* archaeocytes used in **Figure 5C** is
614 composed of all genes enriched between *Spongilla* archaeocytes and other invertebrate
615 stem cells. Note that this set includes genes from other species that are linked by SAMap
616 to the *Spongilla* archeocyte genes. We include genes from other species in the target set
617 to account for differences in KOG functional annotation coverage between species. As
618 such, the annotated transcripts from all 7 species are combined to form the background
619 set. We used a hypergeometric statistical test (Eden et al., 2009) to measure the
620 enrichment of the KOG terms in the target genes compared to the background genes.
621

622 ***Mapping zebrafish and xenopus atlases using existing methods***

623 For benchmarking, we used vertebrate orthologs as determined by Eggnog as input to
624 Harmony (Korsunsky et al., 2019), Liger (Welch et al., 2019), Seurat (Stuart et al., 2019),
625 Scanorama (Hie et al., 2019), BBKNN (Polański et al., 2019), which are all run with default
626 parameters. One-to-one orthologs were selected from one-to-many and many-to-many
627 orthologs by using the bipartite maximum weight matching algorithm implemented in
628 *networkx*. When using the one-to-one orthologs as input for SAMap, we ran for only one
629 iteration. The resulting integrated lower-dimensional coordinates (PCs for Seurat,
630 Harmony, and Scanorama and non-negative matrix factorization coordinates for Liger)
631 and stitched graph (BBKNN and SAMap) were all projected into 2D with UMAP (**Figure
632 2 – figure supplement 2A**). The integrated coordinates are used to generate a nearest
633 neighbor graph using the correlation distance metric, which is then used to compute the

634 alignment scores in **Figure 2 – figure supplement 2B**. The alignment scores for SAMap
635 and BBKNN are directly computed from their combined graphs.
636
637 ***In-situ hybridization in schistosomes***
638 *S. mansoni* (strain: NMRI) juveniles are retrieved from infected female Swiss Webster
639 mice (NR-21963) at ~3 weeks post-infection by hepatic portal vein perfusion using 37°C
640 DMEM supplemented with 5 % heat inactivated FBS. The infected mice are provided by
641 the NIAID Schistosomiasis Resource Center for distribution through BEI Resources, NIH-
642 NIAID Contract HHSN272201000005I. In adherence to the Animal Welfare Act and the
643 Public Health Service Policy on Humane Care and Use of Laboratory Animals, all
644 experiments with and care of mice are performed in accordance with protocols approved
645 by the Institutional Animal Care and Use Committees (IACUC) of Stanford University
646 (protocol approval number 30366). *In situ* hybridization experiments are performed as
647 described previously (Tarashansky et al., 2019), using riboprobes synthesized from gene
648 fragments cloned with the listed primers: collagen (Smp_170340):
649 GGTGAAGAAGGCTGTTGTGG, ACGATCCCCTTTCACTCCTG; tropomyosin
650 (Smp_031770): AAGCTGAAGTCGCCTCACTA, CATATGCCTCTTCACGCTGG;
651 troponin (Smp_018250): CGTAAACCTGGTCAGAAGCG,
652 ATCCTTTTCCTCCAGAGCGT; myosin regulatory light chain (Smp_132670):
653 GAGACAGCGAGTAGTGGAGG, TGCCTTCTTTGATTGGAGCT; wnt (Smp_156540):
654 TGTGGTGATGAAGATGGCAG, CCACGGCCACAACACATATT; frizzled
655 (Smp_174350): CGAACAGGCGCATGACAATA, TGCTAGTCCTGTTGTCGTGT.

Acknowledgments

We thank D. Wagner and C. Juliano for sharing the data and essential discussions. We also thank S. Granick, L. Luo, and J. Kebschull for their critical reading of the manuscript. AJT is a Bio-X Stanford Interdisciplinary Graduate Fellow. This work is supported by a Beckman Young Investigator Award and an NIH grant (1R35GM138061) to BW.

References

Alié, A., Hayashi, T., Sugimura, I., Manuel, M., Sugano, W., Mano, A., Satoh, N., Agata, K., & Funayama, N. (2015). The ancestral gene repertoire of animal stem cells. *Proceedings of the National Academy of Sciences*, *112*(51), E7093–E7100. https://doi.org/10.1073/pnas.1514789112

Arendt, D., Bertucci, P. Y., Achim, K., & Musser, J. M. (2019). Evolution of neuronal types and families. *Current Opinion in Neurobiology*, *56*, 144–152. https://doi.org/10.1016/j.conb.2019.01.022

Arendt, D., Musser, J. M., Baker, C. V. H., Bergman, A., Cepko, C., Erwin, D. H., Pavlicev, M., Schlosser, G., Widder, S., Laubichler, M. D., & Wagner, G. P. (2016). The origin and evolution of cell types. *Nature Reviews Genetics*, *17*(12), 744–757. https://doi.org/10.1038/nrg.2016.127

Barkas, N., Petukhov, V., Nikolaeva, D., Lozinsky, Y., Demharter, S., Khodosevich, K., & Kharchenko, P. V. (2019). Joint analysis of heterogeneous single-cell RNA-seq dataset collections. *Nature Methods*, *16*(8), 695–698. https://doi.org/10.1038/s41592-019-0466-z

Baron, M., Veres, A., Wolock, S. L., Faust, A. L., Gaujoux, R., Vetere, A., Ryu, J. H., Wagner, B. K., Shen-Orr, S. S., Klein, A. M., Melton, D. A., & Yanai, I. (2016). A single-cell transcriptomic map of the human and mouse pancreas reveals inter- and intra-cell population structure. *Cell Systems*, *3*(4), 346-360.e4. https://doi.org/10.1016/j.cels.2016.08.011

Briggs, J. A., Weinreb, C., Wagner, D. E., Megason, S., Peshkin, L., Kirschner, M. W., & Klein, A. M. (2018). The dynamics of gene expression in vertebrate embryogenesis at single-cell resolution. *Science*, *360*(6392), eaar5780. https://doi.org/10.1126/science.aar5780

Brunet, T., Fischer, A. H., Steinmetz, P. R., Lauri, A., Bertucci, P., & Arendt, D. (2016). The evolutionary origin of bilaterian smooth and striated myocytes. *eLife*, *5*, e19607. https://doi.org/10.7554/eLife.19607

Buzgariu, W., Al Haddad, S., Tomczyk, S., Wenger, Y., & Galliot, B. (2015). Multi-functionality and plasticity characterize epithelial cells in *Hydra*. *Tissue Barriers*, *3*(4), e1068908. https://doi.org/10.1080/21688370.2015.1068908

Cao, C., Lemaire, L. A., Wang, W., Yoon, P. H., Choi, Y. A., Parsons, L. R., Matese, J. C., Wang, W., Levine, M., & Chen, K. (2019). Comprehensive single-cell transcriptome lineages of a proto-vertebrate. *Nature*, *571*(7765), 349–354. https://doi.org/10.1038/s41586-019-1385-y

Dubaissi, E., Rousseau, K., Lea, R., Soto, X., Nardeosingh, S., Schweickert, A., Amaya, E., Thornton, D. J., & Papalopulu, N. (2014). A secretory cell type develops alongside multiciliated cells, ionocytes and goblet cells, and provides a protective, anti-infective function in the frog embryonic mucociliary epidermis. *Development*, *141*(7), 1514–1525. https://doi.org/10.1242/dev.102426

Eddy, S. R. (2008). A probabilistic model of local sequence alignment that simplifies statistical significance estimation. *PLoS Computational Biology*, *4*(5), e1000069. https://doi.org/10.1371/journal.pcbi.1000069

Eden, E., Navon, R., Steinfeld, I., Lipson, D., & Yakhini, Z. (2009). GOrilla: A tool for discovery and visualization of enriched GO terms in ranked gene lists. *BMC Bioinformatics*, *10*(1), 48. https://doi.org/10.1186/1471-2105-10-48

El-Brolosy, M. A., Kontarakis, Z., Rossi, A., Kuenne, C., Günther, S., Fukuda, N., Kikhi, K., Boezio, G. L. M., Takacs, C. M., Lai, S.-L., Fukuda, R., Gerri, C., Giraldez, A. J., & Stainier, D. Y. R. (2019). Genetic compensation triggered by mutant mRNA degradation. *Nature*, *568*(7751), 193–197. https://doi.org/10.1038/s41586-019-1064-z

Fincher, C. T., Wurtzel, O., de Hoog, T., Kravarik, K. M., & Reddien, P. W. (2018). Cell type transcriptome atlas for the planarian *Schmidtea mediterranea*. *Science*, *360*(6391), eaaq1736. https://doi.org/10.1126/science.aaq1736

Gabaldón, T., & Koonin, E. V. (2013). Functional and evolutionary implications of gene orthology. *Nature Reviews Genetics*, *14*(5), 360–366. https://doi.org/10.1038/nrg3456

Geirsdottir, L., David, E., Keren-Shaul, H., Weiner, A., Bohlen, S. C., Neuber, J., Balic, A., Giladi, A., Sheban, F., Dutertre, C.-A., Pfeifle, C., Peri, F., Raffo-Romero, A., Vizioli, J., Matiasek, K., Scheiwe, C., Meckel, S., Mätz-Rensing, K., van der Meer, F., … Prinz, M. (2019). Cross-Species Single-Cell Analysis Reveals Divergence of the Primate Microglia Program. *Cell*, *179*(7), 1609-1622.e16. https://doi.org/10.1016/j.cell.2019.11.010

Haghverdi, L., Lun, A. T. L., Morgan, M. D., & Marioni, J. C. (2018). Batch effects in single-cell RNA-sequencing data are corrected by matching mutual nearest neighbors. *Nature Biotechnology*, *36*(5), 421–427. https://doi.org/10.1038/nbt.4091

Hie, B., Bryson, B., & Berger, B. (2019). Efficient integration of heterogeneous single-cell transcriptomes using Scanorama. *Nature Biotechnology*, *37*(6), 685–691. https://doi.org/10.1038/s41587-019-0113-3

Hu, M., Zheng, X., Fan, C.-M., & Zheng, Y. (2020). Lineage dynamics of the endosymbiotic cell type in the soft coral Xenia. *Nature*, *582*(7813), 534–538. https://doi.org/10.1038/s41586-020-2385-7

Huerta-Cepas, J., Serra, F., & Bork, P. (2016). ETE 3: Reconstruction, Analysis, and Visualization of Phylogenomic Data. *Molecular Biology and Evolution*, *33*(6), 1635–1638. https://doi.org/10.1093/molbev/msw046

Huerta-Cepas, J., Szklarczyk, D., Heller, D., Hernández-Plaza, A., Forslund, S. K., Cook, H., Mende, D. R., Letunic, I., Rattei, T., Jensen, L. J., von Mering, C., & Bork, P. (2019). eggNOG 5.0: A hierarchical, functionally and phylogenetically annotated orthology resource based on 5090 organisms and 2502 viruses. *Nucleic Acids Research*, *47*(D1), D309–D314. https://doi.org/10.1093/nar/gky1085

Kalyaanamoorthy, S., Minh, B. Q., Wong, T. K. F., von Haeseler, A., & Jermiin, L. S. (2017). ModelFinder: Fast model selection for accurate phylogenetic estimates. *Nature Methods*, *14*(6), 587–589. https://doi.org/10.1038/nmeth.4285

Korsunsky, I., Millard, N., Fan, J., Slowikowski, K., Zhang, F., Wei, K., Baglaenko, Y., Brenner, M., Loh, P., & Raychaudhuri, S. (2019). Fast, sensitive and accurate integration of single-cell data with Harmony. *Nature Methods*, *16*(12), 1289–1296. https://doi.org/10.1038/s41592-019-0619-0

Larroux, C., Luke, G. N., Koopman, P., Rokhsar, D. S., Shimeld, S. M., & Degnan, B. M. (2008). Genesis and Expansion of Metazoan Transcription Factor Gene Classes. *Molecular Biology and Evolution*, *25*(5), 980–996. https://doi.org/10.1093/molbev/msn047

Laumer, C. E., Hejnol, A., & Giribet, G. (2015). Nuclear genomic signals of the 'microturbellarian' roots of platyhelminth evolutionary innovation. *eLife*, *4*, e05503. https://doi.org/10.7554/eLife.05503

Letunic, I., & Bork, P. (2019). Interactive Tree Of Life (iTOL) v4: Recent updates and new developments. *Nucleic Acids Research*, *47*(W1), W256–W259. https://doi.org/10.1093/nar/gkz239

Li, P., Sarfati, D. N., Xue, Y., Yu, X., Tarashansky, A. J., Quake, S. R., & Wang, B. (2020). *Single-cell analysis of* Schistosoma mansoni *reveals a conserved genetic program controlling germline stem cell fate* [Preprint]. https://doi.org/10.1101/2020.07.06.190033

Littlewood, D. T. J., & Waeschenbach, A. (2015). Evolution: A Turn Up for the Worms. *Current Biology*, *25*(11), R457–R460. https://doi.org/10.1016/j.cub.2015.04.012

Madeira, F., Park, Y. mi, Lee, J., Buso, N., Gur, T., Madhusoodanan, N., Basutkar, P., Tivey, A. R. N., Potter, S. C., Finn, R. D., & Lopez, R. (2019). The EMBL-EBI search and sequence

759 analysis tools APIs in 2019. *Nucleic Acids Research*, *47*(W1), W636–W641.
760 https://doi.org/10.1093/nar/gkz268
761 Malkov, Y. A., & Yashunin, D. A. (2020). Efficient and robust approximate nearest neighbor
762 search using hierarchical navigable small world graphs. *IEEE Transactions on Pattern*
763 *Analysis and Machine Intelligence*, *42*(4), 824–836.
764 https://doi.org/10.1109/TPAMI.2018.2889473
765 Miles, L. B., Darido, C., Kaslin, J., Heath, J. K., Jane, S. M., & Dworkin, S. (2017). Mis-
766 expression of grainyhead-like transcription factors in zebrafish leads to defects in
767 enveloping layer (EVL) integrity, cellular morphogenesis and axial extension. *Scientific*
768 *Reports*, *7*(1), 17607. https://doi.org/10.1038/s41598-017-17898-7
769 Musser, J. M., Schippers, K. J., Nickel, M., Mizzon, G., Kohn, A. B., Pape, C., Hammel, J. U.,
770 Wolf, F., Liang, C., Hernández-Plaza, A., Achim, K., Schieber, N. L., Francis, W. R., Vargas
771 R., S., Kling, S., Renkert, M., Feuda, R., Gaspar, I., Burkhardt, P., … Arendt, D. (2019).
772 *Profiling cellular diversity in sponges informs animal cell type and nervous system evolution*
773 [Preprint]. https://doi.org/10.1101/758276
774 Nehrt, N. L., Clark, W. T., Radivojac, P., & Hahn, M. W. (2011). Testing the ortholog conjecture
775 with comparative functional genomic data from mammals. *PLoS Computational Biology*,
776 *7*(6), e1002073. https://doi.org/10.1371/journal.pcbi.1002073
777 Nguyen, L.-T., Schmidt, H. A., von Haeseler, A., & Minh, B. Q. (2015). IQ-TREE: A fast and
778 effective stochastic algorithm for estimating maximum-likelihood phylogenies. *Molecular*
779 *Biology and Evolution*, *32*(1), 268–274. https://doi.org/10.1093/molbev/msu300
780 Pijuan-Sala, B., Griffiths, J. A., Guibentif, C., Hiscock, T. W., Jawaid, W., Calero-Nieto, F. J.,
781 Mulas, C., Ibarra-Soria, X., Tyser, R. C. V., Ho, D. L. L., Reik, W., Srinivas, S., Simons, B.
782 D., Nichols, J., Marioni, J. C., & Göttgens, B. (2019). A single-cell molecular map of mouse
783 gastrulation and early organogenesis. *Nature*, *566*(7745), 490–495.
784 https://doi.org/10.1038/s41586-019-0933-9
785 Plass, M., Solana, J., Wolf, F. A., Ayoub, S., Misios, A., Glažar, P., Obermayer, B., Theis, F. J.,
786 Kocks, C., & Rajewsky, N. (2018). Cell type atlas and lineage tree of a whole complex
787 animal by single-cell transcriptomics. *Science*, *360*(6391), eaaq1723.
788 https://doi.org/10.1126/science.aaq1723
789 Polański, K., Young, M. D., Miao, Z., Meyer, K. B., Teichmann, S. A., & Park, J.-E. (2019).
790 BBKNN: Fast batch alignment of single cell transcriptomes. *Bioinformatics*, btz625.
791 https://doi.org/10.1093/bioinformatics/btz625
792 Prince, V. E., & Pickett, F. B. (2002). Splitting pairs: The diverging fates of duplicated genes.
793 *Nature Reviews Genetics*, *3*(11), 827–837. https://doi.org/10.1038/nrg928
794 Reddien, P. W. (2018). The Cellular and Molecular Basis for Planarian Regeneration. *Cell*,
795 *175*(2), 327–345. https://doi.org/10.1016/j.cell.2018.09.021
796 Regev, A., Teichmann, S. A., Lander, E. S., Amit, I., Benoist, C., Birney, E., Bodenmiller, B.,
797 Campbell, P., Carninci, P., Clatworthy, M., Clevers, H., Deplancke, B., Dunham, I.,
798 Eberwine, J., Eils, R., Enard, W., Farmer, A., Fugger, L., Göttgens, B., … Human Cell Atlas
799 Meeting Participants. (2017). The Human Cell Atlas. *eLife*, *6*, e27041.
800 https://doi.org/10.7554/eLife.27041
801 Scimone, M. L., Cote, L. E., & Reddien, P. W. (2017). Orthogonal muscle fibres have different
802 instructive roles in planarian regeneration. *Nature*, *551*(7682), 623–628.
803 https://doi.org/10.1038/nature24660
804 Sebé-Pedrós, A., Chomsky, E., Pang, K., Lara-Astiaso, D., Gaiti, F., Mukamel, Z., Amit, I.,
805 Hejnol, A., Degnan, B. M., & Tanay, A. (2018). Early metazoan cell type diversity and the
806 evolution of multicellular gene regulation. *Nature Ecology & Evolution*, *2*(7), 1176–1188.
807 https://doi.org/10.1038/s41559-018-0575-6
808 Shafer, M. E. R. (2019). Cross-Species Analysis of Single-Cell Transcriptomic Data. *Frontiers in*
809 *Cell and Developmental Biology*, *7*, 175. https://doi.org/10.3389/fcell.2019.00175

Siebert, S., Farrell, J. A., Cazet, J. F., Abeykoon, Y., Primack, A. S., Schnitzler, C. E., & Juliano, C. E. (2019). Stem cell differentiation trajectories in *Hydra* resolved at single-cell resolution. *Science*, *365*(6451), eaav9314. https://doi.org/10.1126/science.aav9314

Stamboulian, M., Guerrero, R. F., Hahn, M. W., & Radivojac, P. (2020). The ortholog conjecture revisited: The value of orthologs and paralogs in function prediction. *Bioinformatics*, *36*(Supplement_1), i219–i226. https://doi.org/10.1093/bioinformatics/btaa468

Stuart, T., Butler, A., Hoffman, P., Hafemeister, C., Papalexi, E., Mauck, W. M., Hao, Y., Stoeckius, M., Smibert, P., & Satija, R. (2019). Comprehensive Integration of Single-Cell Data. *Cell*, *177*(7), 1888-1902.e21. https://doi.org/10.1016/j.cell.2019.05.031

Studer, R. A., & Robinson-Rechavi, M. (2009). How confident can we be that orthologs are similar, but paralogs differ? *Trends in Genetics*, *25*(5), 210–216. https://doi.org/10.1016/j.tig.2009.03.004

Tarashansky, A. J., Xue, Y., Li, P., Quake, S. R., & Wang, B. (2019). Self-assembling manifolds in single-cell RNA sequencing data. *eLife*, *8*, e48994. https://doi.org/10.7554/eLife.48994

Tatusov, R. L., Fedorova, N. D., Jackson, J. D., Jacobs, A. R., Kiryutin, B., Koonin, E. V., Krylov, D. M., Mazumder, R., Mekhedov, S. L., Nikolskaya, A. N., Rao, B. S., Smirnov, S., Sverdlov, A. V., Vasudevan, S., Wolf, Y. I., Yin, J. J., & Natale, D. A. (2003). The COG database: An updated version includes eukaryotes. *BMC Bioinformatics*, 14.

Tosches, M. A., & Arendt, D. (2013). The bilaterian forebrain: An evolutionary chimaera. *Current Opinion in Neurobiology*, *23*(6), 1080–1089. https://doi.org/10.1016/j.conb.2013.09.005

Tosches, M. A., Yamawaki, T. M., Naumann, R. K., Jacobi, A. A., Tushev, G., & Laurent, G. (2018). Evolution of pallium, hippocampus, and cortical cell types revealed by single-cell transcriptomics in reptiles. *Science*, *360*(6391), 881–888. https://doi.org/10.1126/science.aar4237

Traag, V. A., Waltman, L., & van Eck, N. J. (2019). From Louvain to Leiden: Guaranteeing well-connected communities. *Scientific Reports*, *9*(1), 5233. https://doi.org/10.1038/s41598-019-41695-z

Wagner, D. E., Weinreb, C., Collins, Z. M., Briggs, J. A., Megason, S., & Klein, A. M. (2018). Single-cell mapping of gene expression landscapes and lineage in the zebrafish embryo. *Science*, *360*(6392), 981–987.

Wang, B., Lee, J., Li, P., Saberi, A., Yang, H., Liu, C., Zhao, M., & Newmark, P. A. (2018). Stem cell heterogeneity drives the parasitic life cycle of Schistosoma mansoni. *eLife*, *7*, e35449. https://doi.org/10.7554/eLife.35449

Weir, K., Dupre, C., van Giesen, L., Lee, A. S.-Y., & Bellono, N. W. (2020). A molecular filter for the cnidarian stinging response. *eLife*, *9*, e57578. https://doi.org/10.7554/eLife.57578

Welch, J. D., Kozareva, V., Ferreira, A., Vanderburg, C., Martin, C., & Macosko, E. Z. (2019). Single-Cell Multi-omic Integration Compares and Contrasts Features of Brain Cell Identity. *Cell*, *177*(7), 1873-1887.e17. https://doi.org/10.1016/j.cell.2019.05.006

Wendt, G. R., & Collins, J. J. (2016). Schistosomiasis as a disease of stem cells. *Current Opinion in Genetics & Development*, *40*, 95–102. https://doi.org/10.1016/j.gde.2016.06.010

Wendt, G. R., Collins, J. N., Pei, J., Pearson, M. S., Bennett, H. M., Loukas, A., Berriman, M., Grishin, N. V., & Collins, J. J. (2018). Flatworm-specific transcriptional regulators promote the specification of tegumental progenitors in Schistosoma mansoni. *eLife*, *7*, e33221. https://doi.org/10.7554/eLife.33221

Wolf, F. A., Angerer, P., & Theis, F. J. (2018). SCANPY: Large-scale single-cell gene expression data analysis. *Genome Biology*, *19*(1), 15. https://doi.org/10.1186/s13059-017-1382-0

Wong, E., Mölter, J., Anggono, V., Degnan, S. M., & Degnan, B. M. (2019). Co-expression of synaptic genes in the sponge Amphimedon queenslandica uncovers ancient neural submodules. *Scientific Reports*, *9*(1), 15781. https://doi.org/10.1038/s41598-019-51282-x

Yan, K.-K., Wang, D., Rozowsky, J., Zheng, H., Cheng, C., & Gerstein, M. (2014). OrthoClust: An orthology-based network framework for clustering data across multiple species. *Genome Biology*, *15*(8), R100. https://doi.org/10.1186/gb-2014-15-8-r100

Zeng, A., Li, H., Guo, L., Gao, X., McKinney, S., Wang, Y., Yu, Z., Park, J., Semerad, C., Ross, E., Cheng, L.-C., Davies, E., Lei, K., Wang, W., Perera, A., Hall, K., Peak, A., Box, A., & Sánchez Alvarado, A. (2018). Prospectively Isolated Tetraspanin+ Neoblasts Are Adult Pluripotent Stem Cells Underlying Planaria Regeneration. *Cell*, *173*(7), 1593-1608.e20. https://doi.org/10.1016/j.cell.2018.05.006

868 **Figures**

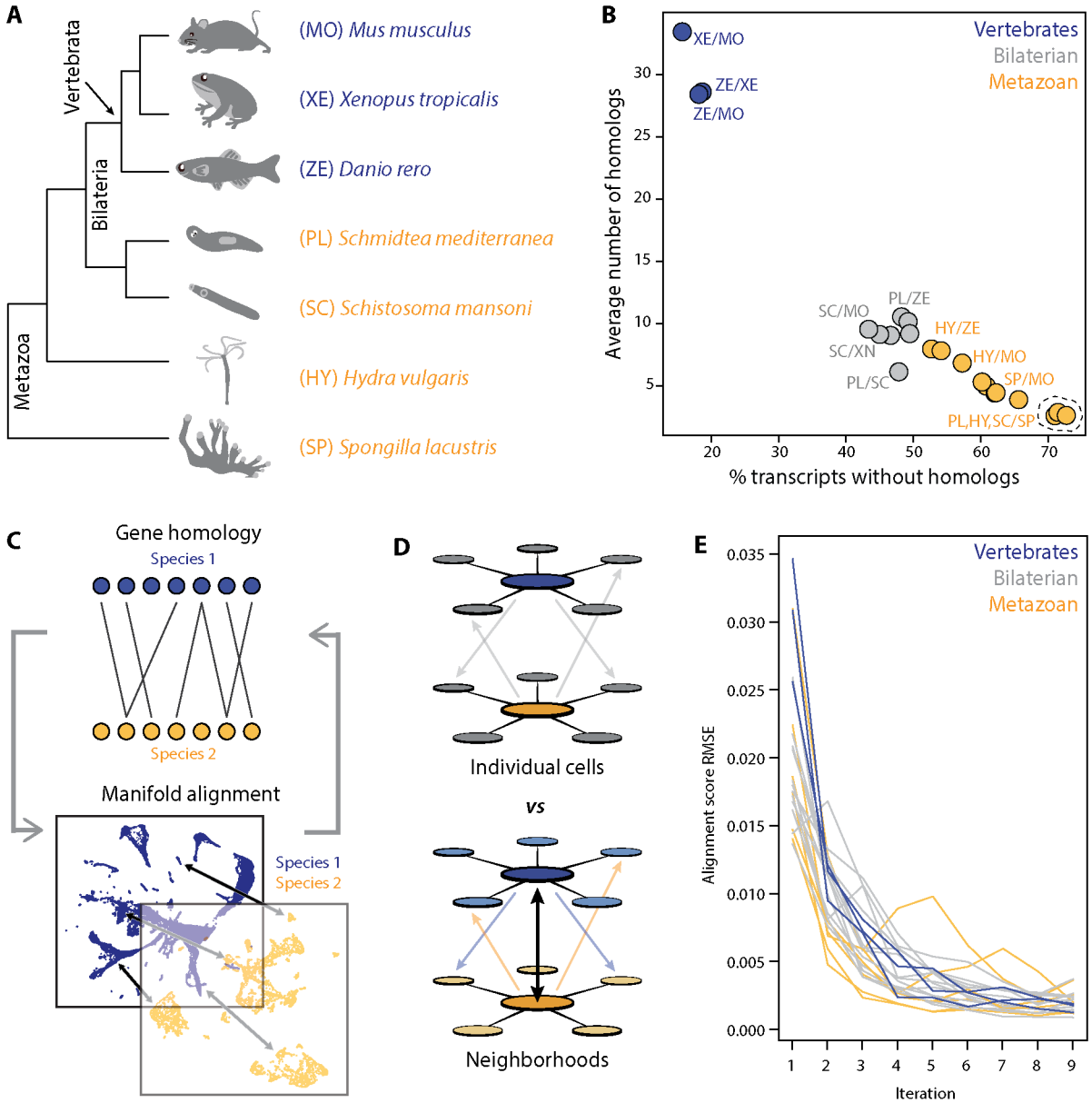

869

870 **Figure 1: SAMap addresses challenges in mapping cell atlases of distantly related**
871 **species.** (A) Schematic showing the phylogenetic relationships among 7 species
872 analyzed. (B) Challenges in mapping single-cell transcriptomes. Gene duplications cause
873 large numbers of homologs per gene, determined by reciprocal BLAST (cut-off: e-value
874 < 10^{-6}), and frequent gene losses and the acquisition of new genes results in large

875 fractions of transcriptomes lacking homology, which limits the amount of information
876 comparable across species. (C) SAMap workflow. Homologous gene pairs initially
877 weighted by protein sequence similarity are used to align the manifolds, low dimensional
878 representations of the cell atlases. Gene-gene correlations calculated from the aligned
879 manifolds are used to update the edge weights in the bipartite graph, which are then used
880 to improve manifold alignment. (D) Mutual nearest neighborhoods improve the detection
881 of cross-species mutual nearest neighbors by connecting cells that target one other's
882 within-species neighborhoods. (E) Convergence of SAMap is evaluated by the root mean
883 square error (RMSE) of the alignment scores between mapped clusters in adjacent
884 iterations for all 21 pairwise comparisons of the 7 species.
885

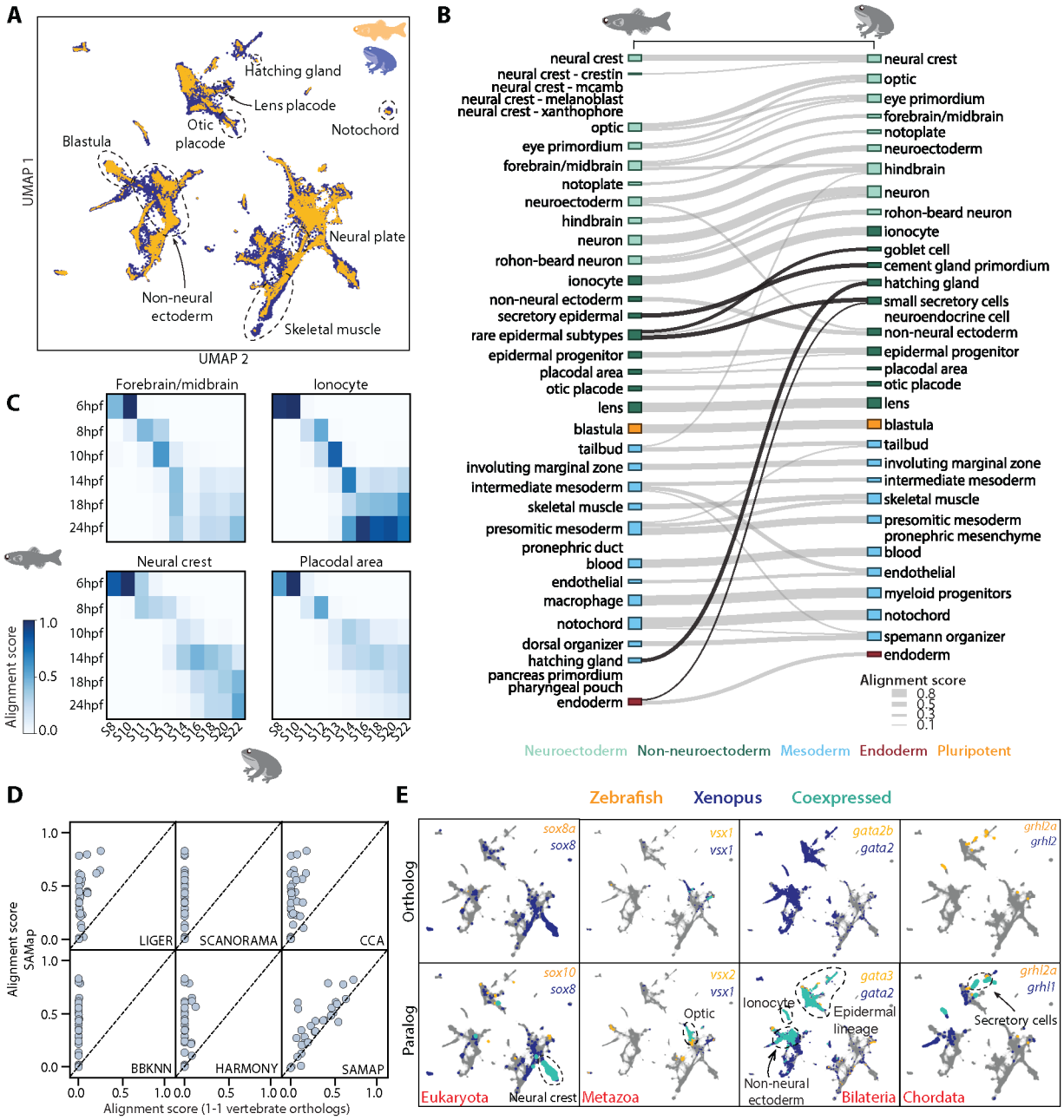

Figure 2: SAMap successfully maps *D. rerio* and *X. tropicalis* atlases and reveals prevalent paralog substitutions. (A) UMAP projection of the combined zebrafish (yellow) and *Xenopus* (blue) manifolds, with example cell types circled. (B) Sankey plot summarizing the cell type mappings. Edges with alignment score < 0.1 are omitted. Edges that connect developmentally distinct secretory cell types are highlighted in black. (C)

892 Heatmaps of alignment scores between developmental time points for ionocyte,
893 forebrain/midbrain, placodal, and neural crest lineages. X-axis: zebrafish. Y-axis:
894 *Xenopus*. (D) SAMap alignment scores compared to those of benchmarking methods
895 using one-to-one vertebrate orthologs as input. Each dot represents a cell type pair
896 supported by ontogeny annotations. (E) Expression of orthologous (left) and paralogous
897 (right) gene pairs overlaid on the combined UMAP projection. Expressing cells are color-
898 coded by species, with those that are connected across species colored cyan. Cells with
899 no expression are shown in gray. More examples are provided in **Figure 2 – figure**
900 **supplement 3**.
901

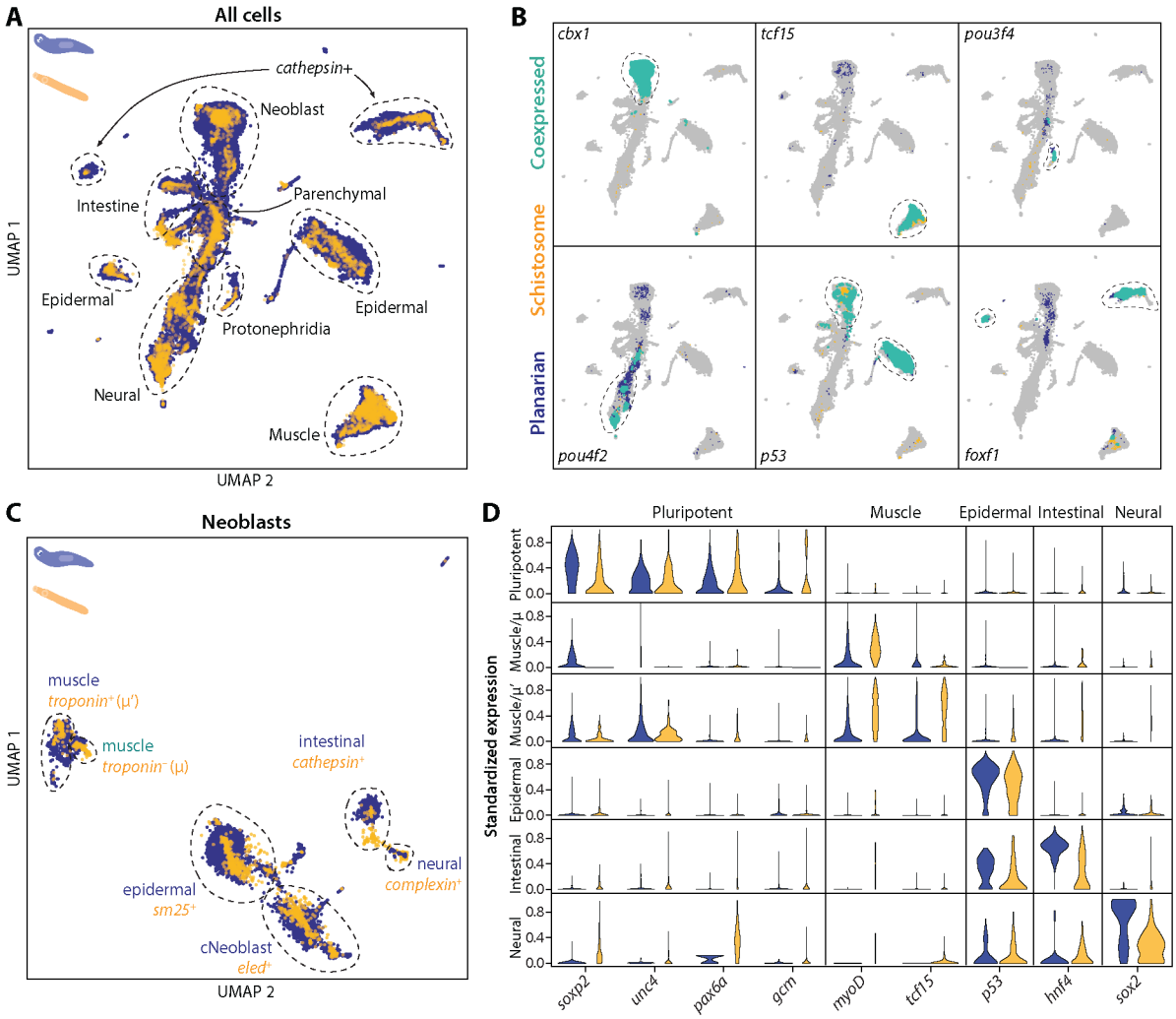

Figure 3: SAMap transfers cell type information from a well-annotated organism (planarian *S. mediterranea*) to its less-studied cousin (schistosome *S. mansoni*) and identifies parallel stem cell compartments. (A) UMAP projection of the combined manifolds. Tissue type annotations are adopted from the *S. mediterranea* atlas (Fincher et al., 2018). The schistosome atlas was collected from juvenile worms, which we found to contain neoblasts with an abundance comparable to that of planarian neoblasts (Li et al., 2020). (B) Overlapping expressions of selected tissue-specific TFs with expressing cell types circled. (C) UMAP projection of the aligned manifolds showing planarian and schistosome neoblasts, with homologous subpopulations circled. Planarian neoblast data

912 is from (Zeng et al., 2018), and cNeoblasts correspond to the Nb2 population, which are
913 pluripotent cells that can rescue neoblast-depleted planarians in transplantation
914 experiments. (D) Distributions of conserved TF expressions in each neoblast
915 subpopulation. Expression values are *k*-nearest-neighbor averaged and standardized,
916 with negative values set to zero. Blue: planarian; yellow: schistosome.
917

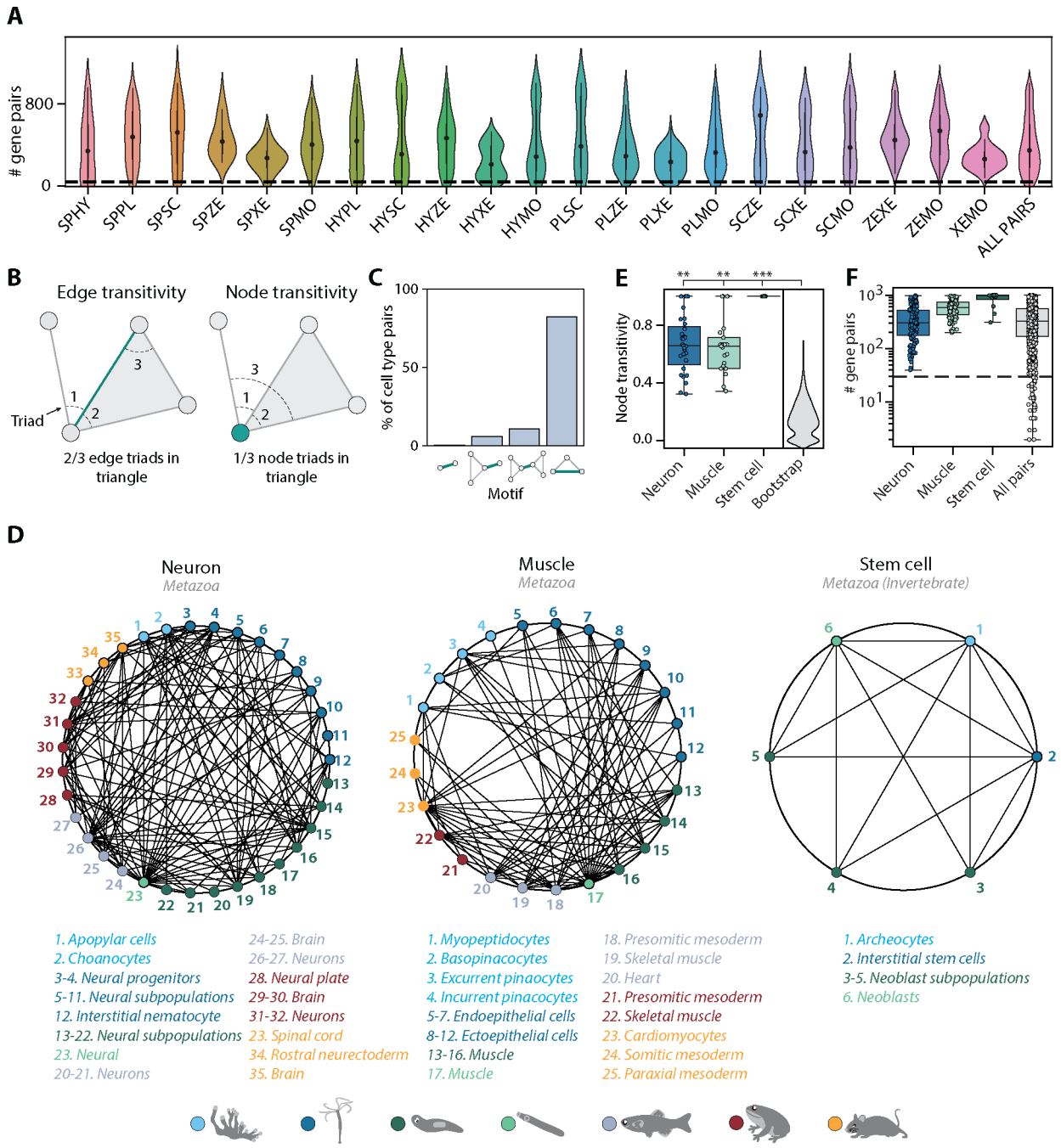

Figure 4: Mapping evolutionarily distant species identifies densely connected cell type groups. (A) Violin plots showing the number of enriched gene pairs in cell type mappings from all 21 pairwise mappings between the 7 species. 87% of cell type mappings have greater than 40 enriched gene pairs (dotted line). Species acronyms are

923 the same as in **Figure 1A**. (B) Schematic illustrating edge (left) and node (right)
924 transitivities, defined as the fraction of triads (set of three connected nodes) in closed
925 triangles. (C) The percentage of cell type pairs that are topologically equivalent to the
926 green edge in each illustrated motif. (D) Network graphs showing highly connected cell
927 type families. Each node represents a cell type, color-coded by species (detailed
928 annotations are provided in **Supplementary Table 5**). Mapped cell types are connected
929 with an edge. (E) Boxplot showing the median and interquartile ranges of node
930 transitivities for highly connected cell type groups. For all box plots, the whiskers denote
931 the maximum and minimum observations. The average node transitivity per group is
932 compared to a bootstrapped null transitivity distribution, generated by repeatedly
933 sampling subsets of nodes in the cell type graph and calculating their transitivities. *$p <$
934 $5x10^{-3}$, ** $p < 5x10^{-5}$, ***$p < 5x10^{-7}$. (F) Boxplot showing the median and interquartile
935 ranges of the number of enriched gene pairs in highly connected cell type groups. All cell
936 type connections in these groups have at least 40 enriched gene pairs (dotted line).

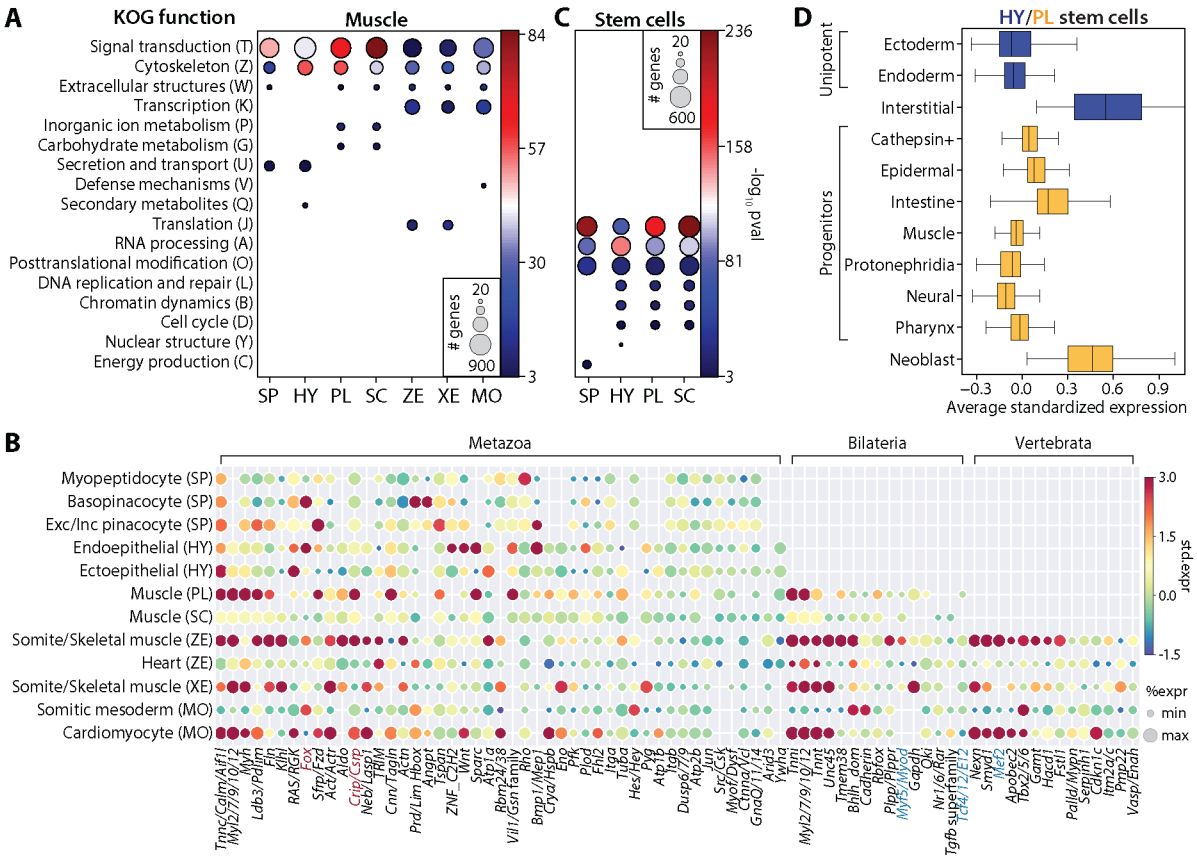

937

938 **Figure 5: SAMap identifies muscle and stem cell transcriptional signatures**
939 **conserved across species.** (A) Enrichment of KOG functional annotations calculated
940 for genes shared in contractile cell types. For each species, genes enriched in individual
941 contractile cell types are combined. (B) Expression and enrichment of conserved muscle
942 genes in contractile cell types. Color: mean standardized expression. Symbol size: the
943 fraction of cells each gene is expressed in per cell type. Homologs are grouped based on
944 overlapping eukaryotic Eggnog orthology groups. If multiple genes from a species are
945 contained within an orthology group, the gene with highest standardized expression is
946 shown. Genes in blue: core transcriptional program of bilaterian muscles; red:
947 transcription factors conserved throughout Metazoa. (C) Enrichment of KOG functional
948 annotations for genes shared by stem cell types. (D) Boxplot showing the median and

949 interquartile ranges of the mean standardized expressions of genes in hydra and
950 planarian stem cells/progenitors that are conserved across all invertebrate species in this
951 study. Planarian progenitors: *piwi*+ cells that cluster with differentiated tissues in Fincher
952 et al. (Fincher et al., 2018). Neoblasts: cluster 0 in Fincher et al. (Fincher et al., 2018) that
953 does not express any tissue-specific markers.
954

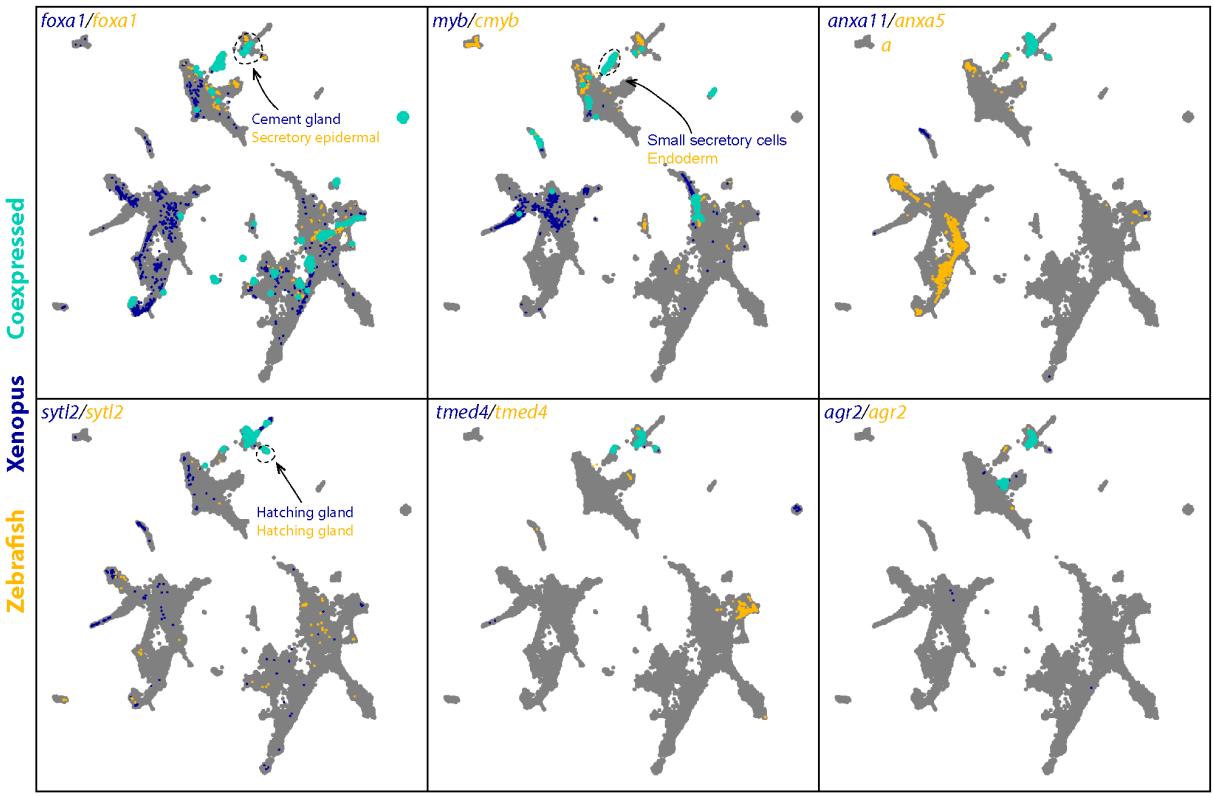

955

956 **Figure 2 – figure supplement 1: Expression of selected genes enriched in *D. rerio***

957 **and *X. tropicalis* secretory cell types.** Expressions of orthologous gene pairs linked by

958 SAMap are overlaid on the combined UMAP projection. Expressing cells are color-coded

959 by species, with those connected across species colored cyan. Cells with no expression

960 are shown in gray. The mapped secretory cell types are highlighted with circles.

961

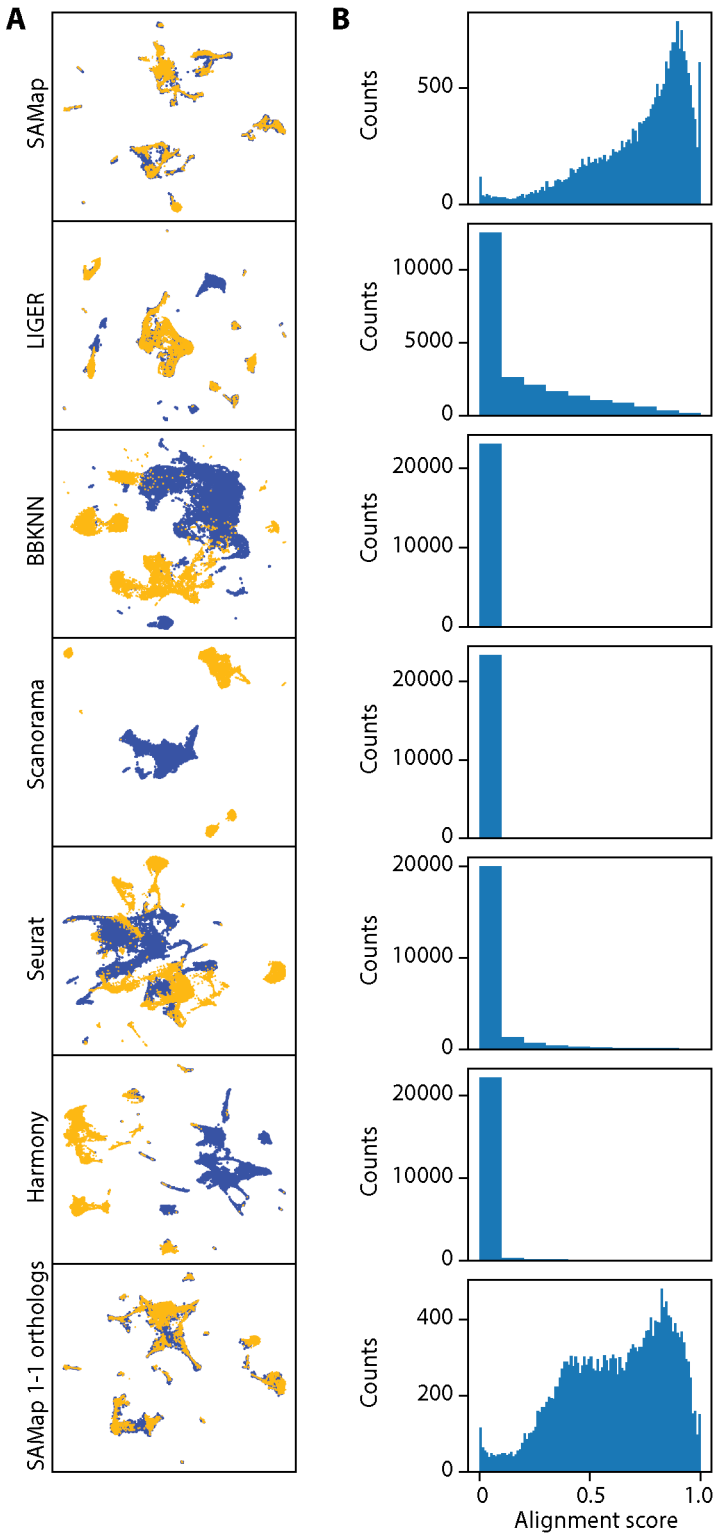

962

963 **Figure 2 – figure supplement 2: Existing methods failed to map *D. rerio* and *X.***

964 ***tropicalis* atlases.** (A) UMAP projections of the integration results from SAMap using the

965 full homology graph, compared to Liger, BBKNN, Scanorama, Seurat, Harmony, and
966 SAMap using 1-1 orthologs. For fair comparisons, all methods were run on the *D. rerio*
967 and *X. torpicalis* atlases subsampled to approximately 15,000 cells to satisfy
968 computational constraints of Seurat and Liger. (B) Distribution of alignment scores
969 between individual cells.
970

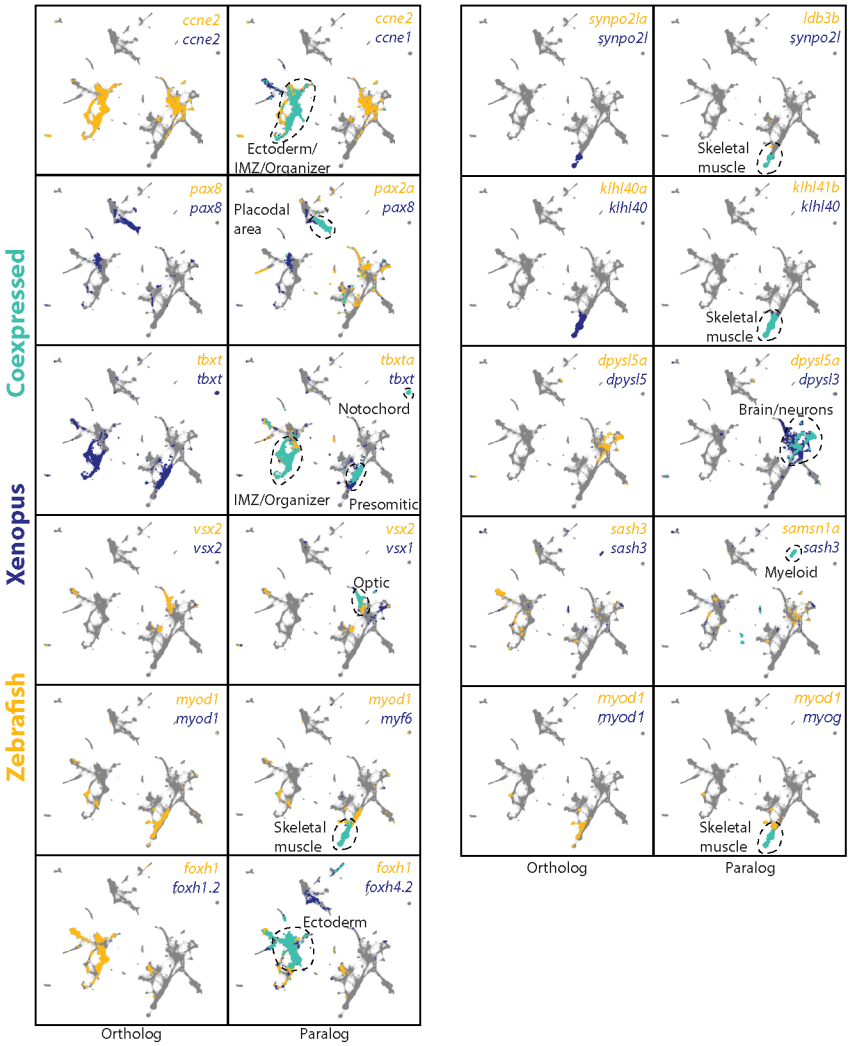

971

972 **Figure 2 – figure supplement 3: Representative examples of paralog substitution**
973 **events in *D. rerio* and *X. tropicalis* atlases.** Expressions of orthologous and paralogous
974 gene pairs are overlaid on the combined UMAP projection. Expressing cells are color-
975 coded by species, with those that are connected across species colored in cyan. Cells
976 with no expression are shown in gray.

977

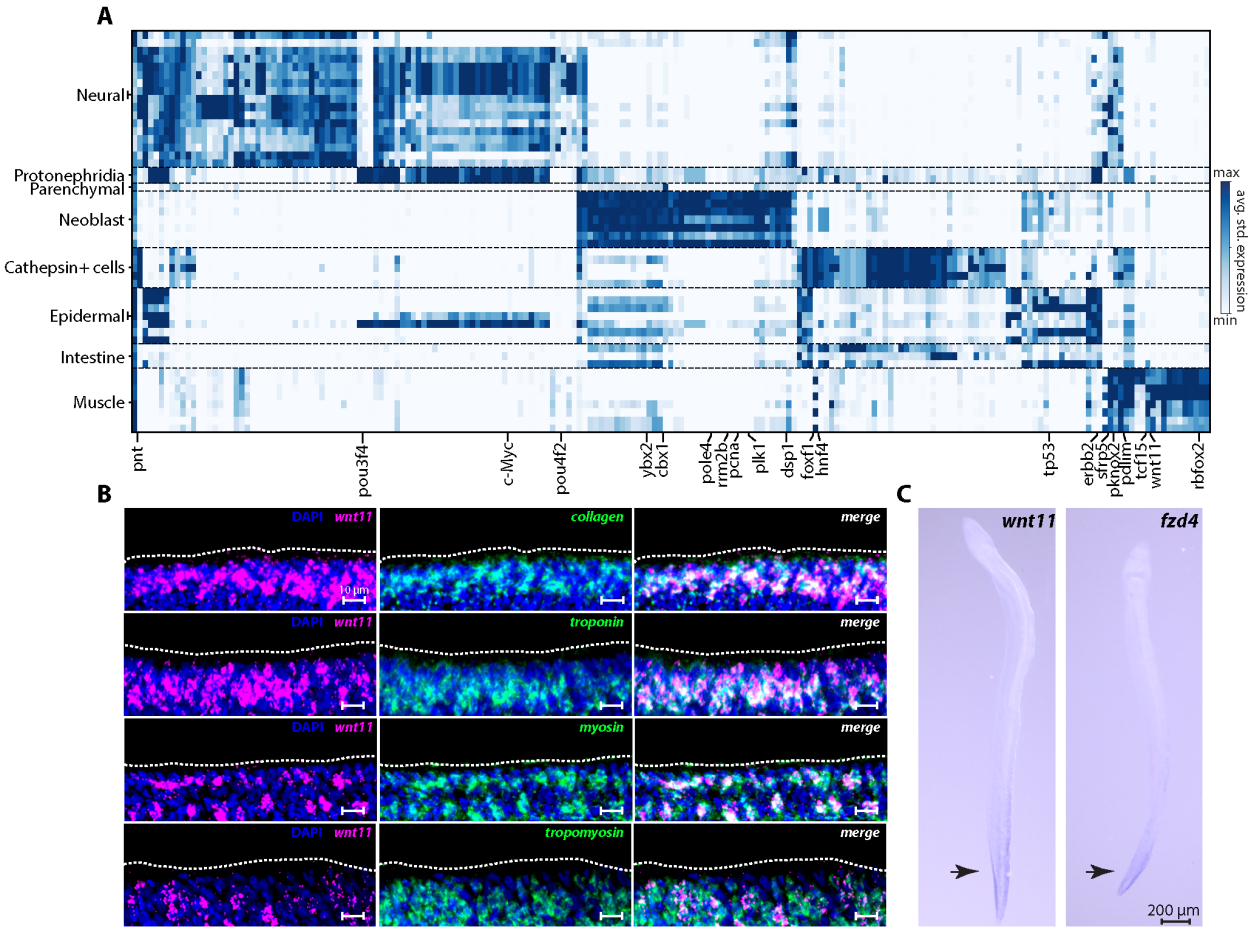

Figure 3 – figure supplement 1: **SAMap-linked gene pairs that are enriched in cell type pairs between *S. mediterranea* and *S. mansoni*.** (A) Rows: linked cell types. Schistosome cell types correspond to leiden clusters. Columns: genes linked by SAMap with overlapping eukaryotic Eggnog orthology groups. We calculate the average standardized expression of each gene in an orthology group for its corresponding cell type in a particular pair and report the highest expression. A selected set of orthology groups corresponding to transcriptional regulators are labeled. (B) Fluorescence *in situ* hybridization shows the co-expression of *wnt* (Smp_156540) and a panel of muscle markers (*collagen*, *troponin*, *myosin* and *tropomyosin*) in *S. mansoni* juveniles. The body wall muscles are expected to be located close to the parasite surface (dashed outline).

989 The images are maximum intensity projections constructed from ~10 confocal slices with
990 optimal axial spacing recommended by the Zen software collected on a Zeiss LSM 800
991 confocal microscope using a 40× (N.A. = 1.1, working distance = 0.62 mm) water-
992 immersion objective (LD C-Apochromat Corr M27). (C) Whole mount *in situ* hybridization
993 images showing that the expression of *wnt* and *frizzled* (Smp_174350) are concentrated
994 in the parasite tail (arrows) with decreasing gradients extending anteriorly. In planarian
995 muscles, Wnt genes provide the positional cues for setting up the body plan during
996 regeneration (Scimone et al., 2017; Reddien, 2018). The presence of an anterior-
997 posterior expression gradient of *wnt* and *frizzled* in muscles of schistosome juveniles
998 suggests that they may have similar functional roles in patterning during development.
999

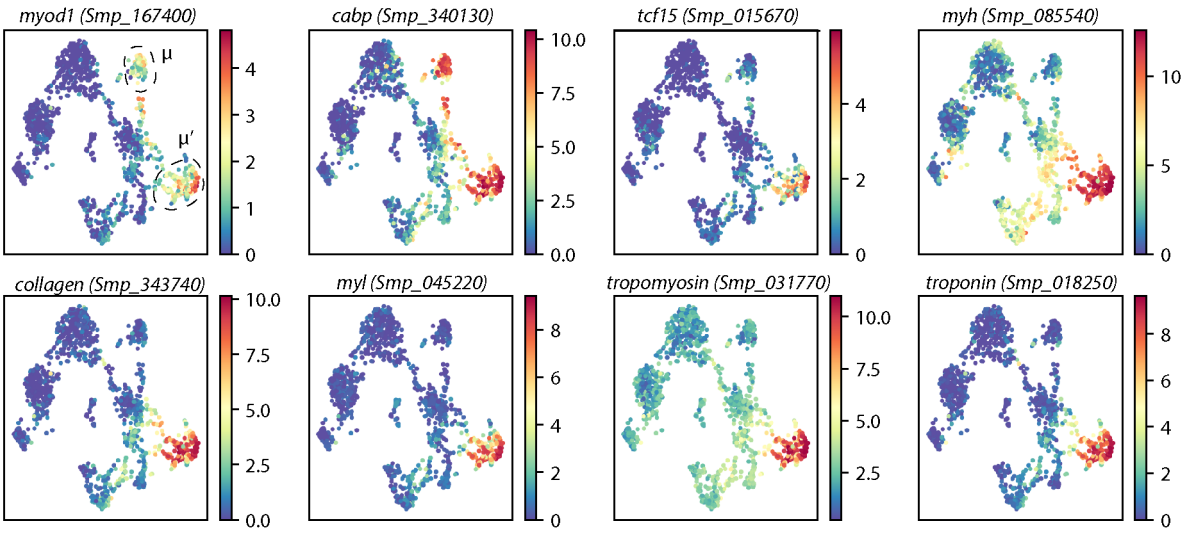

Figure 3 – figure supplement 2: Schistosome neoblasts express canonical muscle markers in muscle progenitors. UMAP projections of schistosome neoblasts with gene expressions overlaid. μ and μ' cells are circled. Colormap: expression in units of $log_2(D + 1)$. For visualization, expression was smoothed via nearest-neighbor averaging using SAM. Note that *myod1* and *cabp* are expressed in both presumptive muscle progenitor populations, whereas all other markers are enriched in μ' cells. All genes displayed are also expressed in fully differentiated muscle tissues.

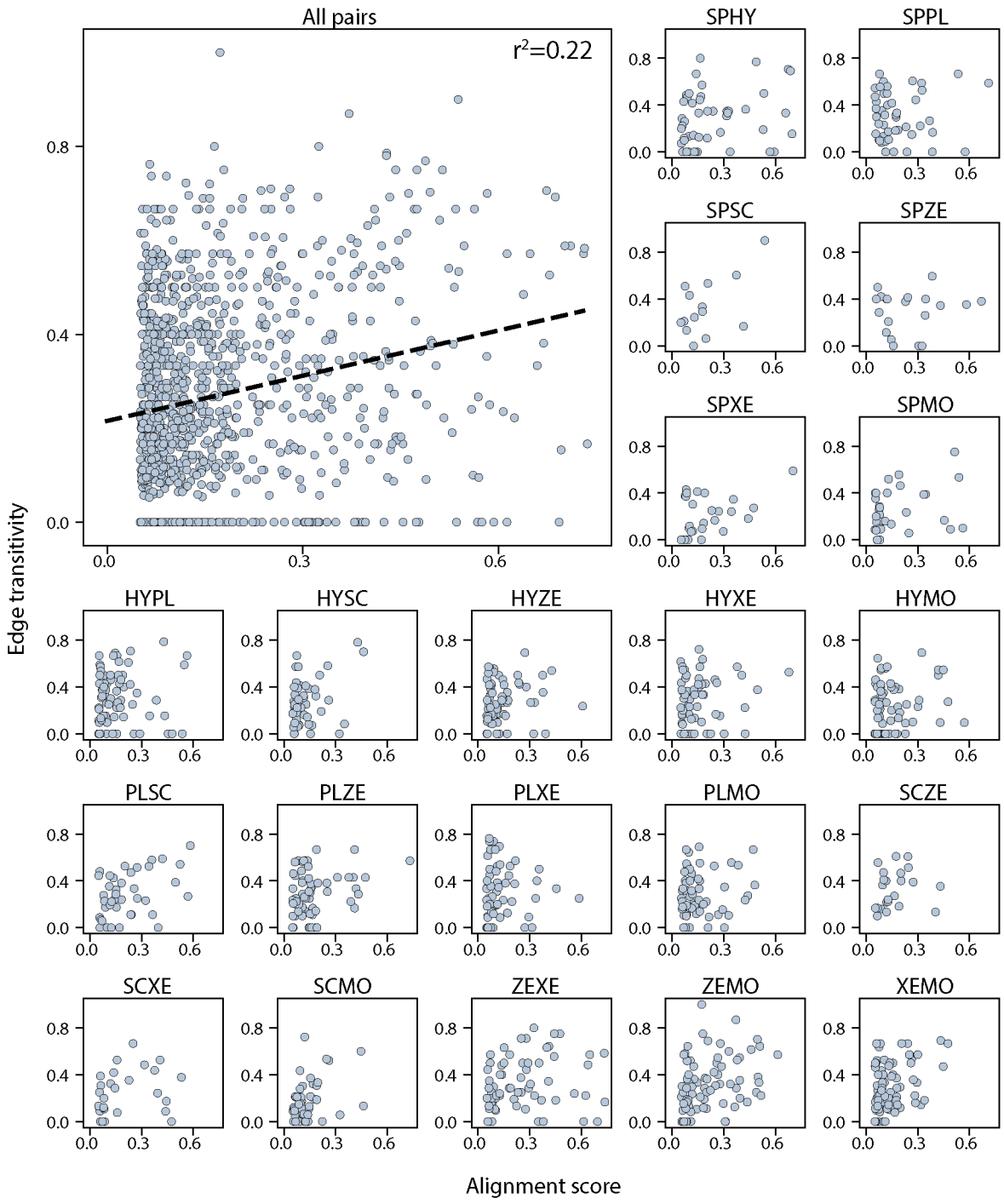

1009

1010 **Figure 4 – figure supplement 1**: **Alignment scores are mostly independent of edge**

1011 **transitivity.** Top left: alignment scores and edge transitivity for all cell type pairs in the

1012 connectivity graph including the 7 species. Dotted line: the linear best fit, with the Pearson

correlation coefficient reported at the top. Alignment scores and edge transitivity for individual species pairs are shown in the remaining subplots.

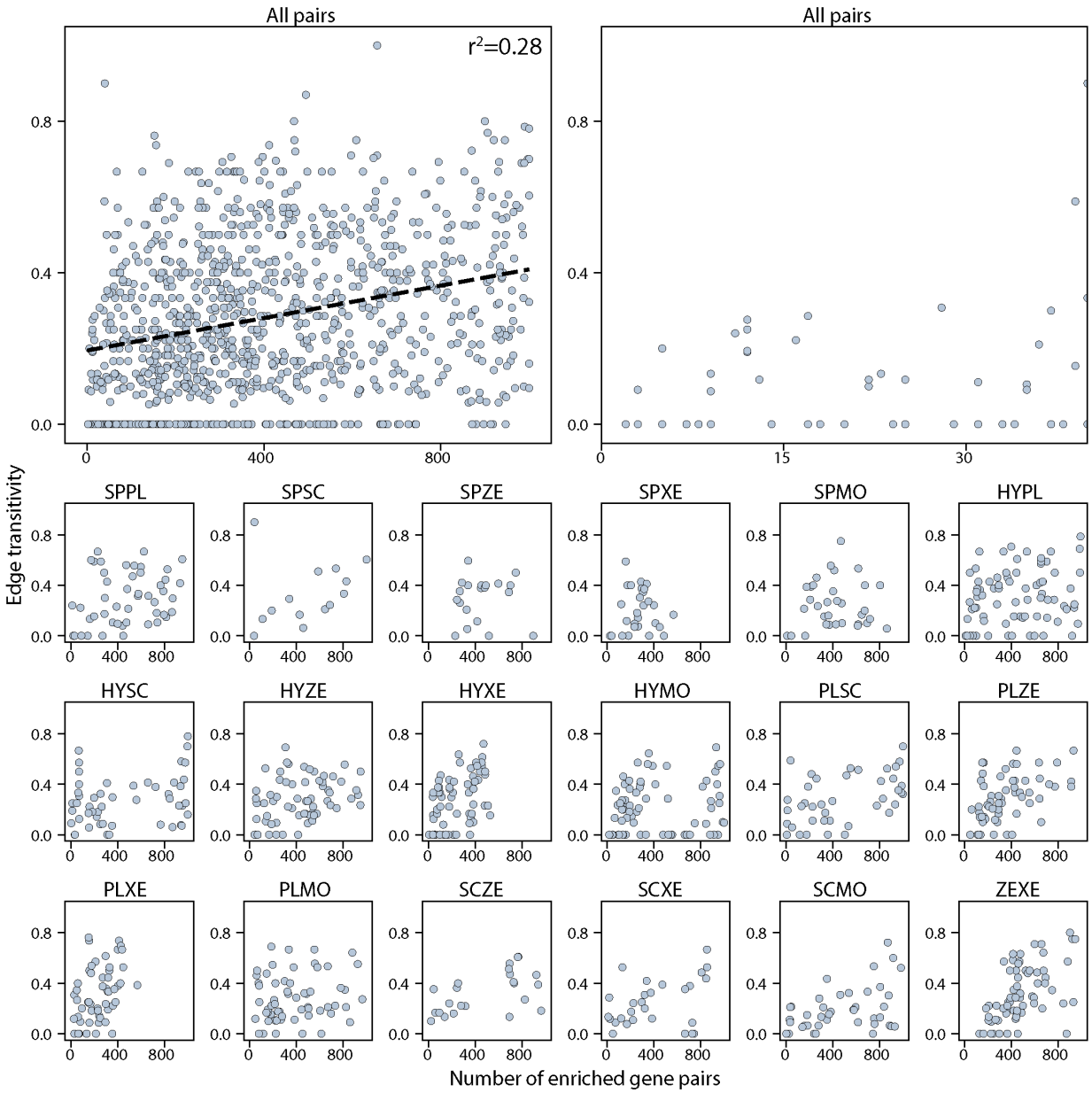

Figure 4 – figure supplement 2: **Number of enriched gene pairs are mostly independent of edge transitivity.** Top left: The edge transitivity is plotted against the number of enriched gene pairs for all cell type pairs in the connectivity graph. Dotted line: the linear best fit, with the Pearson correlation coefficient reported at the top. Top right: magnified view of the mapped cell type pairs supported by small numbers of gene pairs

1022 (<40) to show those edges have low transitivity scores (<0.4). The sublots below show

1023 the number of enriched gene pairs and edge transitivity for individual species pairs.

1024

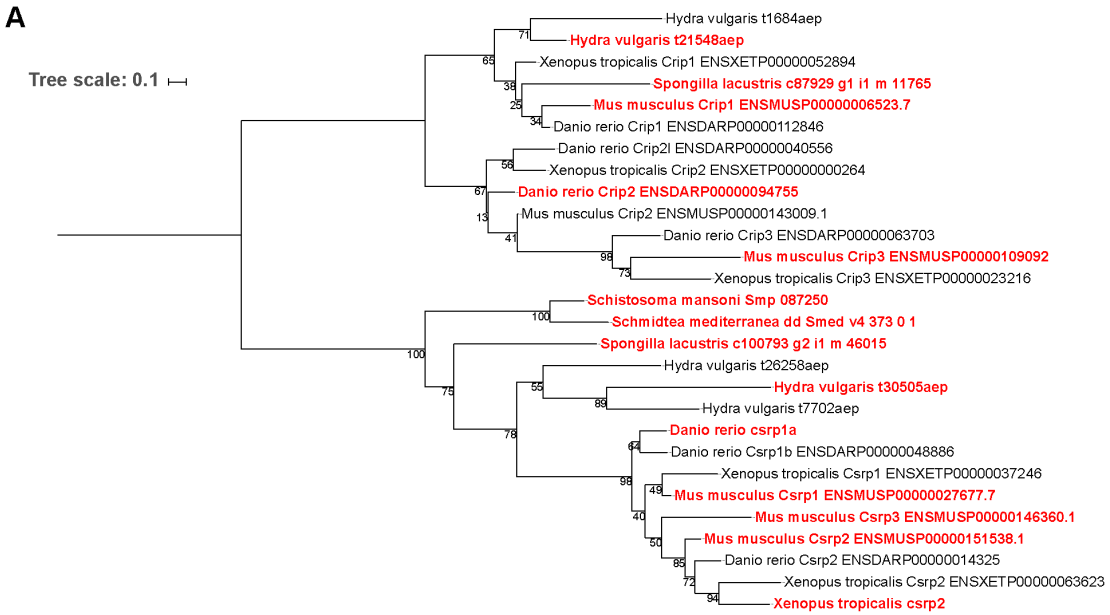
A
Tree scale: 0.1
Hydra vulgaris t1684aep
Hydra vulgaris t21548aep
Xenopus tropicalis Crip1 ENSXETP00000052894
Spongilla lacustris c87929 g1 i1 m 11765
Mus musculus Crip1 ENSMUSP00000006523.7
Danio rerio Crip1 ENSDARP00000112846
Danio rerio Crip2l ENSDARP00000040556
Xenopus tropicalis Crip2 ENSXETP00000000264
Danio rerio Crip2 ENSDARP00000094755
Mus musculus Crip2 ENSMUSP00000143009.1
Danio rerio Crip3 ENSDARP00000063703
Mus musculus Crip3 ENSMUSP00000109092
Xenopus tropicalis Crip3 ENSXETP00000023216
Schistosoma mansoni Smp 087250
Schmidtea mediterranea dd Smed v4 373 0 1
Spongilla lacustris c100793 g2 i1 m 46015
Hydra vulgaris t26258aep
Hydra vulgaris t30505aep
Hydra vulgaris t7702aep
Danio rerio csrp1a
Danio rerio Csrp1b ENSDARP00000048886
Xenopus tropicalis Csrp1 ENSXETP00000037246
Mus musculus Csrp1 ENSMUSP00000027677.7
Mus musculus Csrp3 ENSMUSP00000146360.1
Mus musculus Csrp2 ENSMUSP00000151538.1
Danio rerio Csrp2 ENSDARP00000014325
Xenopus tropicalis Csrp2 ENSXETP00000063623
Xenopus tropicalis csrp2

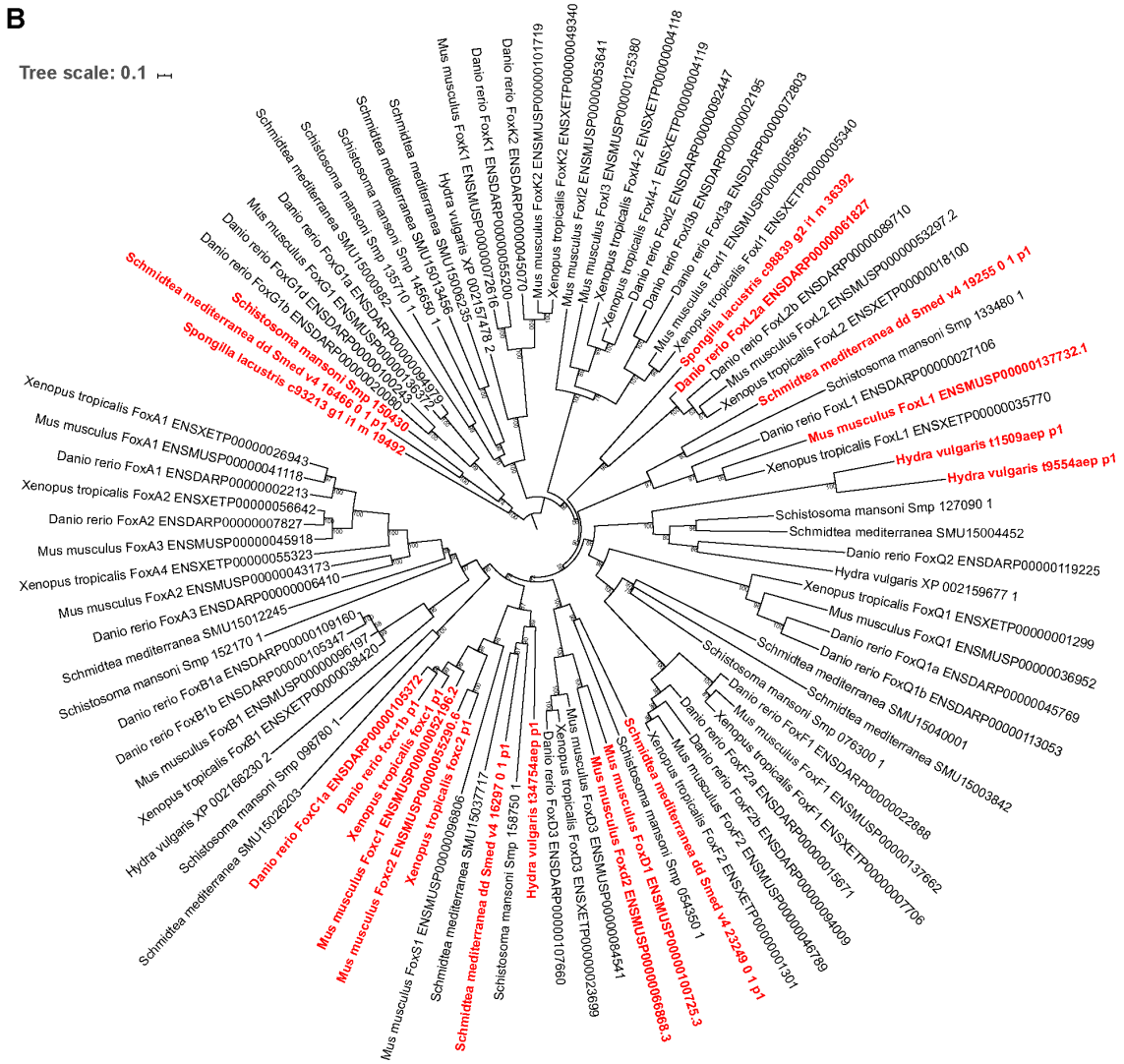
B
Tree scale: 0.1
Xenopus tropicalis FoxA1 ENSXETP00000026943
Mus musculus FoxA1 ENSMUSP00000041118
Danio rerio FoxA1 ENSDARP00000002213
Xenopus tropicalis FoxA2 ENSXETP00000056642
Danio rerio FoxA2 ENSDARP00000007827
Mus musculus FoxA3 ENSMUSP00000045918
Xenopus tropicalis FoxA4 ENSXETP00000055323
Mus musculus FoxA2 ENSMUSP00000006410
Danio rerio FoxA3 ENSDARP00000043173
Schmidtea mediterranea SMU15012245
Schistosoma mansoni Smp 152170 1
Danio rerio FoxB1a ENSDARP00000109160
Danio rerio FoxB1b ENSDARP00000105347
Mus musculus FoxB1 ENSMUSP00000096197
Xenopus tropicalis FoxB1 ENSXETP00000038420
Hydra vulgaris XP 002166230 2
Schistosoma mansoni Smp 098780 1
Schmidtea mediterranea SMU15026203
Schmidtea mediterranea dd Smed v4 16466 0 1 p1
Schistosoma mansoni Smp 159430
Spongilla lacustris c93213 g1 i1 m 19492
Danio rerio FoxC1a ENSDARP00000105372
Danio rerio foxc1b p1
Xenopus tropicalis foxc1 p1
Mus musculus FoxC1 ENSMUSP00000052136.2
Mus musculus FoxC2 ENSMUSP00000053290.6
Xenopus tropicalis foxc2 p1
Schmidtea mediterranea dd Smed v4 16297 0 1 p1
Hydra vulgaris t34754aep p1
Mus musculus FoxS1 ENSMUSP00000096806
Schmidtea mediterranea SMU15037117
Schistosoma mansoni Smp 158750 1
Schmidtea mediterranea SMU15006235
Danio rerio FoxK1 ENSMUSP00000072616
Danio rerio FoxK2 ENSDARP00000055200
Mus musculus FoxK1 ENSMUSP00000101719
Xenopus tropicalis FoxK2 ENSXETP00000049340
Mus musculus FoxK2 ENSMUSP00000053641
Xenopus tropicalis FoxI3 ENSMUSP00000125380
Mus musculus FoxI3 ENSMUSP00000004118
Danio rerio FoxI4-1 ENSXETP00000004119
Danio rerio FoxI4-2 ENSDARP00000092447
Danio rerio FoxI2 ENSDARP00000002195
Danio rerio FoxI3b ENSDARP00000072803
Danio rerio FoxI3a ENSDARP00000058651
Mus musculus FoxI1 ENSMUSP00000005340
Xenopus tropicalis FoxI1 ENSXETP00000061827
Spongilla lacustris c98839 g2 i1 m 36392
Danio rerio FoxL2a ENSDARP00000089710
Danio rerio FoxL2b ENSDARP00000053297.2
Mus musculus FoxL2 ENSMUSP00000018100
Xenopus tropicalis FoxL2 ENSXETP00000027106
Schmidtea mediterranea dd Smed v4 19255 0 1 p1
Schistosoma mansoni Smp 133480 1
Danio rerio FoxL1 ENSDARP00000035770
Mus musculus FoxL1 ENSMUSP00000137732.1
Xenopus tropicalis FoxL1 ENSXETP00000036952
Hydra vulgaris t1509aep p1
Hydra vulgaris t9554aep p1
Schistosoma mansoni Smp 127090 1
Schmidtea mediterranea SMU15004452
Danio rerio FoxQ2 ENSDARP00000119225
Hydra vulgaris XP 002159677 1
Xenopus tropicalis FoxQ1 ENSXETP00000001299
Mus musculus FoxQ1 ENSMUSP00000045769
Danio rerio FoxQ1a ENSDARP00000113053
Danio rerio FoxQ1b ENSDARP00000022888
Schmidtea mediterranea SMU15040001
Schmidtea mediterranea SMU15003842
Schistosoma mansoni Smp 076300 1
Danio rerio FoxF1 ENSDARP00000137662
Mus musculus FoxF1 ENSMUSP00000007706
Xenopus tropicalis FoxF1 ENSXETP00000015871
Xenopus tropicalis FoxF2a ENSDARP00000094009
Danio rerio FoxF2b ENSDARP00000046789
Mus musculus FoxF2 ENSMUSP00000001301
Xenopus tropicalis FoxF2 ENSXETP00000023699
Schmidtea mediterranea dd Smed v4 23249 0 1 p1
Schistosoma mansoni Smp 054350 1
Mus musculus FoxD1 ENSMUSP00000100725.3
Mus musculus FoxD2 ENSMUSP00000066868.3
Schmidtea mediterranea dd Smed v4 23249 0 1 p1
Mus musculus FoxD3 ENSMUSP00000084541
Xenopus tropicalis FoxD3 ENSXETP00000023699
Danio rerio FoxD3 ENSDARP00000107660

1025

1026 **Figure 5 – figure supplement 1: Phylogenetic reconstruction of animal contractile**
1027 **cell transcriptional regulators.** Trees depict *Csrp/Crip* (A) and Fox group I (B) gene
1028 families. Genes labelled red are enriched in at least one contractile gene pair identified
1029 via SAMap. Support values indicate bootstrap support from 1,000 nonparametric (*Csrp*)
1030 or ultrafast (*Fox*) bootstrap replicates. Besides these two transcriptional regulators,
1031 contractile cells in all seven species were found to be also enriched for transcription
1032 factors from the C2H2 Zinc Finger, Lim Homeobox, and Paired Homeobox families,
1033 although in different cell types we found enrichment of a number of distinct orthologs.
1034 Whether this reflects an ancestral role for these transcription factor families in regulating
1035 contractility or their independent evolution will require additional taxonomic sampling and
1036 broader coverage of muscle cell diversity to resolve.

1037 **Supplementary table captions**

1038

1039 **Supplementary Table 1: Cell atlas metadata and cell annotations.** Metadata includes
1040 the number of cells, number of transcripts in the transcriptome, median number of
1041 transcripts detected per cell, the reference transcriptome used in this study, database
1042 through which the transcriptomes are provided, technology used for constructing the cell
1043 atlases, atlas data accessions, processing notes, and references. Leiden clusters and
1044 cell type annotations are reported for cells in each atlas. The Zebrafish and *Xenopus*
1045 tables include both the original cell type annotations and those used in this study. *D. rerio*,
1046 *X. tropicalis*, and mouse annotations include developmental stages.

1047

1048 **Supplementary Table 2: Cell type annotations for the zebrafish-*Xenopus* mapping.**
1049 Correspondence between the cell type annotations provided in the original study (Briggs
1050 et al., 2018; Wagner et al., 2018) and corresponding annotations used in this study is
1051 provided for both *D. rerio* and *X. tropicalis* atlases.

1052

1053 **Supplementary Table 3: Identified paralogs with greater expression similarity than**
1054 **orthologs in the zebrafish-*Xenopus* mapping.** Each row contains a pair of vertebrate-
1055 orthologous genes and a corresponding pair of eukaryotic paralogs with higher correlation
1056 in expression compared to the orthologs, the expression correlations for ortholog and
1057 paralog pairs, the difference between their correlations, and whether the paralogs are
1058 considered as a paralog substitution (defined as when the substituted ortholog is either

1059 absent or lowly-expressed with no cell-type specificity). Highlighted rows are shown in
1060 **Figure 2E** and **Figure 2 – figure supplement 3**.
1061
1062 **Supplementary Table 4: Genes enriched in contractile cell types and invertebrate**
1063 **stem cells highlighted in Figure 4D.** The IDs of the genes enriched in the contractile
1064 and invertebrate stem cell types are provided along with the IDs of the Eggnog orthology
1065 groups to which they belong. In cases where multiple genes from a species belonging to
1066 the same orthology group are enriched, the most differentially expressed gene is shown.
1067 The descriptions in the stem cell table are orthology annotations associated with the
1068 *Spongilla* genes provided in the original study (Musser et al., 2019).
1069
1070 **Supplementary Table 5: Cell types in the cell type families shown in Figure 4D.** For
1071 the schistosome cell types, we annotated two neural clusters, both of which express the
1072 neural marker *complexin* (Li et al., 2020). One of the clusters expresses the antigen
1073 *SmKK7*, so we label the clusters “Neural” and “Neural_KK7”, respectively. The “Muscle”
1074 population contains non-neoblast cells expressing *troponin*. The “Tegument_prog” and
1075 “Tegument” populations consist of cells expressing tegument progenitor and
1076 differentiated marker genes, respectively, as reported in a previous study (Wendt et al.,
1077 2018).